

¹ Physics-Infused Reduced-Order Modeling for Analysis of
² Ablating Hypersonic Thermal Protection Systems

³

⁴ November 17, 2025

⁵

Abstract

⁶ This work presents a *physics-infused reduced-order modeling* (PIROM) framework
⁷ towards the design, analysis, and optimization of non-decomposing ablating hyper-
⁸ sonic thermal protection systems (TPS). It is demonstrated via the modeling of trans-
⁹ient thermo-ablative behavior of non-decomposing multi-layered hypersonic TPS. The
¹⁰ PIROM architecture integrates a reduced-physics backbone, based on the lumped-
¹¹ capacitance model (LCM), with data-driven correction dynamics formulated via a
¹² coarse-graining approach rooted in the Mori-Zwanzig formalism. The LCM is coupled
¹³ to a surface recession model (SRM) to capture the recession of the ablating TPS as a
¹⁴ function of the surface temperature. While the LCM and SRM capture the dominant
¹⁵ physics of the ablating TPS response, the correction terms compensate for residual
¹⁶ dynamics arising from higher-order non-linear interactions and heterogeneities across
¹⁷ material layers. The PIROM consistently achieves errors of $\approx 0.5\%$ for a wide range of
¹⁸ extrapolative settings of design parameters involving time-and-space varying bound-
¹⁹ary conditions and SRM models, and improves by an order of magnitude by the LCM
²⁰ alone. Moreover, the PIROM delivers online evaluations that are two orders of magni-
²¹tude faster than the full-order model (FOM). These results demonstrate that PIROM
²² effectively reconciles the trade-offs between accuracy, generalizability, and efficiency,
²³ providing a promising framework for optimizing multi-physical dynamical systems,
²⁴ such as TPS under diverse operating conditions.

²⁵

1 Introduction

²⁶ At hypersonic speeds, aerospace vehicles experience extreme aero-thermo-dynamic environ-
²⁷ments that require specialized thermal protection systems (TPS) to shield internal sub-
²⁸structures, electronics, and possibly crew members from the intense aerodynamic heating.
²⁹ The TPS is often composed of ablating materials – a high-temperature capable fibrous
³⁰ material injected with a resin that fills the pore network and strengthens the compos-
³¹ite Amar2016. The TPS design promotes the exchange of mass through thermal and
³²chemical reactions (i.e., pyrolysis), effectively mitigating heat transfer to the sub-structures.

³³ As a result, accurate prediction for the ablating TPS response under extreme hyper-
³⁴sonic heating becomes fundamental to ensuring survivability, performance, and safety of

35 hypersonic vehicles. Not only is it necessary to assess the performance of the thermal management systems, but also the shape changes of the vehicle's outer surface induced by the
36 ablating material, and its impact on the aerodynamics, structural integrity, and controllability.
37 Nonetheless, high-fidelity simulations of ablating TPS remains a formidable challenge
38 both theoretically and computationally.
39

40 Unfortunately, high-fidelity simulations of ablating TPS remains a formidable challenge
41 both theoretically and computationally.

42 On the theoretical side, the thermo-chemical reactions, coupled with the irregular pore
43 network structure, translate into simplifying assumptions to reduce non-linearities, and make
44 the resulting equations more amenable for engineering application and design analysis **x**.
45 For instance, one of the most notable codes is the one-dimensional **CMA** code that was
46 developed by Aerotherm Corporation in the 1960s **Howard2015**. Despite its practical use
47 in...

48 Another example is the CHarring Ablator Response (CHAR) ablation code, which ignores
49 elemental decompositions of the pyrolyzing gases, assumes the gases to be a mixture of perfect
50 gases in thermal equilibrium, and assumes no reaction or condensation with the porous
51 network [1].

52 In sum, the objectives of this work are as follows:

- 53 1. Extend the previous PIROM formulation in Ref. [13] to model transient thermo-
54 ablative response of multi-layered hypersonic TPS through a systematic coarse-graining
55 procedure based on the Mori-Zwanzig formalism.
- 56 2. Benchmark the accuracy, generalizability, and computational accelerations of the PIROM
57 against the RPM and the high-fidelity FEM solutions of ablating TPS, thus assessing
58 the PIROM's capabilities to solve the ITM in complex multi-physical non-linear dy-
59 namical systems.

60 2 Modeling of Ablating Thermal Protection Systems

61 This section presents the problem of modeling a non-decomposing ablating TPS subjected to
62 extreme hypersonic heating. Two different but mathematically connected solution strategies
63 are provided: (1) a high-fidelity full-order model (FOM) based on a finite element method
64 (FEM), and (2) a low-fidelity reduced-physics model (RPM) based on a lumped capacitance
65 model (LCM) and a one-dimensional surface velocity model (SRM). The FOM is compu-
66 tationally expensive but provides the highest fidelity, while the RPM is computationally
67 efficient but has low predictive fidelity; both models are amenable to high-dimensional de-
68 sign variables. The RPM is used in the subsequent sections for deriving the PIROM.

69 2.1 Governing Equations

70 The multi-physics for a non-decomposing ablating TPS involves the *energy equation* which
71 models the transient heat conduction inside the TPS, and the *pseudo-elasticity equation*,
72 which models the mesh motion due to surface recession. The governing PDEs for the ablating
73 TPS are summarized in this section.

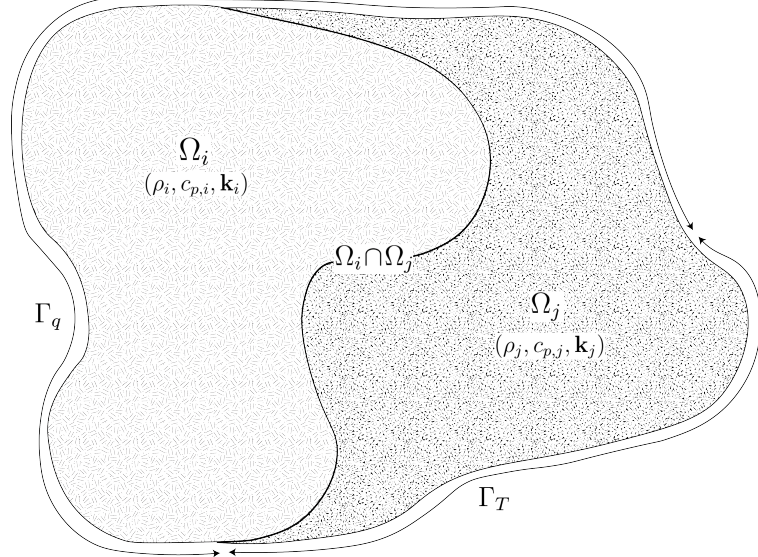


Figure 1: General domain Ω with prescribed Neumann and Dirichlet boundary conditions on Γ_q and Γ_T . Mesh displacement $w(x, t)$ occurs on the Γ_q boundary.

74 2.1.1 Energy Equation

75 Consider a generic domain $\Omega \subset \mathbb{R}^d$, $d = 2$ or 3 , illustrated in Fig. 1. Let $\partial\Omega = \Gamma_q \cup \Gamma_T$ and
 76 $\Gamma_q \cap \Gamma_T = \emptyset$, where a Neumann $q_b(x, t)$ boundary condition is prescribed on the Γ_q boundary,
 77 and represents the surface exposed to the hypersonic boundary layer. The Dirichlet $T_b(x, t)$
 78 boundary condition is prescribed on the boundary Γ_T . The TPS is divided into N non-
 79 overlapping components $\{\Omega_i\}_{i=1}^N$, as illustrated in Fig. 1 for $N = 2$. The i -th component Ω_i
 80 is associated with material properties $(\rho_i, c_{p,i}, \mathbf{k}_i)$, that are assumed to be continuous within
 81 one component, and can be discontinuous across two neighboring components.

82 The transient heat conduction is described by the energy equation,

$$74 \quad \rho c_p \left(\frac{\partial T}{\partial t} + \tilde{\mathbf{v}}(x, t) \cdot \nabla T \right) - \nabla \cdot (\mathbf{k} \nabla T) = 0, \quad x \in \Omega \quad (1a)$$

$$75 \quad -\mathbf{k} \nabla T \cdot \mathbf{n} = q_b(x, t), \quad x \in \Gamma_q \quad (1b)$$

$$76 \quad T(x, t) = T_b(x, t), \quad x \in \Gamma_T \quad (1c)$$

$$77 \quad T(x, 0) = T_0(x), \quad x \in \Omega \quad (1d)$$

83 where the density ρ is constant, while the heat capacity c_p and thermal conductivity $\mathbf{k} \in \mathbb{R}^{d \times d}$
 84 may depend on temperature. In the order they appear, the terms in eq. (1a) include, the
 85 unsteady energy storage, heat conduction, temperature advection due to mesh motion, and
 86 source terms due to boundary conditions. The boundary conditions for the energy equation
 87 includes Neumann eq. (1b) and Dirichlet eq. (1c) on Γ_T .

88 An Arbitrary Lagrangian-Eulerian (ALE) description is used to account for mesh motion
 89 due to surface recession, where $\tilde{\mathbf{v}}(x, t)$ is the relative velocity of the material with respect to
 90 the mesh,

$$89 \quad \tilde{\mathbf{v}}(x, t) = \mathbf{v}_s(x, t) - \mathbf{v}_m(x, t) \quad (2)$$

91 where $\mathbf{v}_s(x, t)$ and $\mathbf{v}_m(x, t)$ are the physical material velocity and mesh velocity, respectively.
 92 In this work, the physical material velocity is assumed to be zero, i.e., $\mathbf{v}_s(x, t) = \mathbf{0}$, and thus
 93 the relative velocity is simply the negative of the mesh velocity, $\tilde{\mathbf{v}}(x, t) = -\mathbf{v}_m(x, t)$.

94 2.1.2 Pseudo-Elasticity Equation

95 The mesh motion is described by the steady-state pseudo-elasticity equation without body
 96 forces,

$$\nabla \cdot \boldsymbol{\sigma}(\mathbf{w}) = \mathbf{0}, \quad \forall t \in \mathcal{T}, \mathbf{x} \in \Omega \quad (3a)$$

$$\mathbf{w}(\mathbf{x}, t) = \mathbf{w}_q(\mathbf{x}, t), \quad \forall t \in \mathcal{T}, \mathbf{x} \in \Gamma_q \quad (3b)$$

$$\mathbf{w}(\mathbf{x}, t) = \mathbf{0}, \quad \forall t \in \mathcal{T}, \mathbf{x} \notin \Gamma_q \quad (3c)$$

$$\mathbf{w}(\mathbf{x}, 0) = \mathbf{0}, \quad \forall \mathbf{x} \in \Omega \quad (3d)$$

97 where the stress tensor $\boldsymbol{\sigma}$ is related to the strain tensor $\boldsymbol{\epsilon}(\mathbf{w})$ through Hooke's law,

$$\boldsymbol{\sigma}(\mathbf{w}) = \mathbb{D} : \boldsymbol{\epsilon}(\mathbf{w})$$

98 where \mathbb{D} is the fourth-order positive definite elasticity tensor, and “:” is the double con-
 99 traction of the full-order tensor \mathbb{D} with the second-order tensor $\boldsymbol{\epsilon}$. The elasticity tensor
 100 ordinarily possess a number of symmetries, effectively reducing the number of components
 101 that describe it [2]. The symmetric strain tensor $\boldsymbol{\epsilon}$ measures the deformation of the mesh
 102 due to displacements $\mathbf{w}(x, t)$, and is defined as,

$$\boldsymbol{\epsilon}(\mathbf{w}) = \frac{1}{2} (\nabla \mathbf{w} + \nabla \mathbf{w}^\top)$$

103 The “material” properties for the mesh are chosen to tailor the mesh deformation, and need
 104 not represent the actual material being modeled [1].

105 For the pseudo-elasticity equations, the boundary conditions include prescribed displace-
 106 ments $\mathbf{w}_q(x, t)$ on the heated boundary Γ_q in eq. (3b), and zero displacements on the unheated
 107 boundaries in eq. (3c). The initial condition for the mesh displacements is zero in eq. (3d).
 108 Particularly, the surface velocity due to the ablating material is a function of the surface
 109 temperature $T_q(x, t)$ for $x \in \Gamma_q$ on the heated boundary. For the i -th material component,
 110 the mesh velocity on the heated boundary is imposed based on the following relation,

$$\hat{\mathbf{n}} \cdot \mathbf{v}_m(x, t) = f(T_q(x, t)), \quad x \in \Gamma_q \quad (4)$$

111 where $\hat{\mathbf{n}}$ is the unit normal vector on the heated boundary Γ_q , and f is a function obtained
 112 from tabulated data for the material, commonly referred to as a B' table [1]. The B' table
 113 provides a model for the recession velocity as a function of the surface temperature, and is
 114 pre-computed based on high-fidelity simulations of the ablation process for a one-dimensional
 115 slab of the material, and is independent of the TPS geometry. Provided the surface velocity,
 116 the boundary condition in eq. (5) for the mesh displacements are computed by integrating

¹¹⁷ the surface velocity over time,

$$\mathbf{w}_q(x, t) = \int_0^t \mathbf{v}_m(x, \tau) d\tau \quad (5)$$

¹¹⁸ 2.2 Full-Order Model: Finite-Element Method

¹¹⁹ To obtain the full-order numerical solution, the *energy equation* is spatially discretized using
¹²⁰ variational principles of the Discontinuous Galerkin (DG) method [5]. Note that the choice
¹²¹ of DG approach is mainly for theoretical convenience, and is exclusively performed on the
¹²² energy equation, as it is the surface temperature that drives the ablation process. The
¹²³ equivalence between DG and FEM is noted upon their convergence. For the *pseudo-elasticity*
¹²⁴ *equation* standard FEM is used to compute the mesh displacements based on the surface
¹²⁵ temperature provided by the DG solution of the energy equation [2].

¹²⁶ Consider a conforming mesh partition domain, where each element belongs to one and
¹²⁷ only one component. Denote the collection of all M elements as $\{E_i\}_{i=1}^M$. In an element E_i ,
¹²⁸ its shared boundaries with another element E_j , Neumann BC, and Dirichlet BC are denoted
¹²⁹ as e_{ij} , e_{iq} , and e_{iT} , respectively. Lastly, $|e|$ denotes the length ($n_d = 2$) or area ($n_d = 3$) of a
¹³⁰ component boundary e .

¹³¹ For the i -th element, use a set of P trial functions, such as polynomials, to represent the
¹³² temperature distribution,

$$T_i(x, t) = \sum_{l=1}^P \phi_l^i(x) u_l^i(t) \equiv \boldsymbol{\phi}_i^\top(x) \mathbf{u}_i(t), \quad i = 1, 2, \dots, M \quad (6)$$

¹³³ Without loss of generality, the trial functions are assumed to be orthogonal, so that,

$$\int_{E_i} \phi_l^i(x) \phi_k^i(x) d\Omega = 0, \quad l \neq k$$

¹³⁴ where δ_{lk} is the Kronecker delta function. Furthermore, for simplicity, choose $\phi_1^i = 1$. Thus,
¹³⁵ by orthogonality,

$$\int_{E_i} \phi_1^i(x) d\Omega = |E_i|, \quad \int_{E_i} \phi_k^i(x) d\Omega = 0, \quad k = 2, 3, \dots, P$$

¹³⁶ Under the choice of basis functions, u_1^i is simply the average temperature of element E_i ,
¹³⁷ denoted as \bar{u}_i .

¹³⁸ By standard variational processes, e.g., [5], the element-wise governing equation is de-
¹³⁹ noted as,

$$\mathbf{A}_i \dot{\mathbf{u}}_i = (\mathbf{B}_i + \mathbf{C}_i) \mathbf{u}_i + \sum_{j \in \mathcal{N}_i \cup \{T_b\}} (\mathbf{B}_{ij}^i \mathbf{u}_i + \mathbf{B}_{ij}^j \mathbf{u}_j) + \mathbf{f}_i(t), \quad \text{for } i = 1, 2, \dots, M \quad (7)$$

¹⁴⁰ which is collected as the following ODE for the all the elements in the mesh,

$$\mathbf{A}(\mathbf{u})\dot{\mathbf{u}} = [\mathbf{B}(\mathbf{u}) + \mathbf{C}(\mathbf{u})]\mathbf{u} + \mathbf{f}(t) \quad (8)$$

¹⁴¹ where $\mathbf{u} = [\mathbf{u}_1, \mathbf{u}_2, \dots, \mathbf{u}_M]^\top \in \mathbb{R}^{MP}$ includes all the DG variables, $\mathbf{f} \in \mathbb{R}^{MP}$ is the exten-
¹⁴² sional forcing, and the system matrices \mathbf{A} , \mathbf{B} , and \mathbf{C} are the matrices due to heat capacity,
¹⁴³ heat conduction, and temperature advection due to mesh motion, respectively. A detailed
¹⁴⁴ derivation of eqs. (7) and (8) and their matrices is provided in Appendix A.

¹⁴⁵ 2.3 Reduced-Physics Model

¹⁴⁶ The RPM for predicting the response of the ablating TPS consists of two components: (1) the
¹⁴⁷ *lumped-capacitance model* (LCM), and (2) the *surface recession model* (SRM). The LCM is
¹⁴⁸ described as a first-order system of ODEs for predicting the average temperatures inside the
¹⁴⁹ components of the TPS, and provides a low-fidelity (under estimate) for the component's
¹⁵⁰ surface temperature. The SRM provides a relation between the surface temperature and
¹⁵¹ the surface recession velocity based on pre-computed B' tables for the material, enabling the
¹⁵² computation of one-dimensional surface displacements. The LCM and SRM are combined to
¹⁵³ define the RPM, providing low-fidelity estimates for the temperatures and surface recession
¹⁵⁴ of the ablating TPS.

¹⁵⁵ 2.3.1 Lumped Capacitance Model

¹⁵⁶ A general form of the LCM is provided in this section; details regarding the derivation
¹⁵⁷ for the four-component TPS used in the results section are provided in Appendix A. The
¹⁵⁸ LCM is a classical physics-based low-order model for predicting the temporal variation of
¹⁵⁹ average temperature in multiple interconnected components [7]. The LCM is derived at the
¹⁶⁰ component level from a point of view of energy conservation, and leads to the following
¹⁶¹ system of ODEs for the average temperatures on the components,

$$\bar{\mathbf{A}}\dot{\bar{\mathbf{u}}} = \bar{\mathbf{B}}\bar{\mathbf{u}} + \bar{\mathbf{f}}(t) \quad (9)$$

¹⁶² Where the states and inputs,

$$\bar{\mathbf{u}} = [\bar{u}_1, \bar{u}_2, \dots, \bar{u}_N]^\top \in \mathbb{R}^N, \quad \bar{\mathbf{f}} = [\bar{f}_1, \bar{f}_2, \dots, \bar{f}_N]^\top \in \mathbb{R}^N \quad (10)$$

¹⁶³ include the average temperatures $\bar{\mathbf{u}}$ and spatially-integrated inputs $\bar{\mathbf{f}}$ for the N components.
¹⁶⁴ For $i, j = 1, 2, \dots, N$ the (i, j) -th elements of the $\bar{\mathbf{A}} \in \mathbb{R}^{N \times N}$, $\bar{\mathbf{B}} \in \mathbb{R}^{N \times N}$, and $\bar{\mathbf{f}} \in \mathbb{R}^N$
¹⁶⁵ matrices are given by,

$$\bar{A}_i = \begin{cases} \int_{\Omega_i} \rho c_p d\Omega_i, & i = j \\ 0, & i \neq j \end{cases}, \quad \bar{B}_{ij} = \begin{cases} \sum_{j \in \mathcal{N}_i \cup \{T_b\}} \bar{B}_{ij}^i, & i = j \\ \bar{B}_{ij}^{(j)}, & i \neq j \end{cases}, \quad (11a)$$

$$\bar{\mathbf{f}}_i = \begin{cases} |e_{iq}| \bar{q}_i + \frac{|e_{iT}|}{R_i} \bar{T}_i, & i = j \\ 0, & i \neq j \end{cases} \quad (11b)$$

¹⁶⁶ where,

$$\bar{q}_i = \frac{1}{|e_{iq}|} \int_{e_{iq}} q_b de_{iq}, \quad \bar{T}_i = \frac{1}{|e_{iT}|} \int_{e_{iT}} T_b de_{iT}, \quad \bar{B}_{ij}^i = -\frac{|e_{ij}|}{R_{ij}}, \quad \bar{B}_{ij}^j = \frac{|e_{ij}|}{R_{ij}} \quad (12)$$

¹⁶⁷ where R_{ij} is the equivalent thermal resistance between two neighboring components Ω_i and
¹⁶⁸ Ω_j , and R_i is the thermal resistance between component Ω_i and the Dirichlet boundary.
¹⁶⁹ The thermal resistances are computed based on the geometry and material properties of the
¹⁷⁰ components; details regarding their computation are provided in Appendix A.

¹⁷¹ 2.3.2 Surface Recession Model

¹⁷² The displacement is assumed to be *one-dimensional* on the heated boundary Γ_q , i.e., the
¹⁷³ surface recedes only in the direction of the applied load. Displacements perpendicular to
¹⁷⁴ the direction of the applied load are assumed small and are neglected. Thus, for the i -th
¹⁷⁵ ablating component, the one-dimensional SRM considered in this work takes the form,

$$\dot{\mathbf{w}} = \boldsymbol{\Xi} \bar{\mathbf{u}} - \tilde{\mathbf{f}} \quad (13)$$

¹⁷⁶ where $\boldsymbol{\Xi} = \text{diag}(\alpha_1, \dots, \alpha_{\tilde{N}})$ and $\tilde{\mathbf{f}} = (\alpha_1 \bar{u}_{0,1}, \dots, \alpha_{\tilde{N}} \bar{u}_{0,\tilde{N}})^\top$. The constants α_i are small
¹⁷⁷ material-dependent constants, determined from the B' table, and $\bar{u}_{0,i}$ is the constant initial
¹⁷⁸ temperature of the ablative component. The SRM provides a relation between the surface's
¹⁷⁹ temperature and recession velocity, based on pre-computed B' tables for the material.

¹⁸⁰ 2.3.3 Thermo-Ablative Reduced-Physics Model

¹⁸¹ The LCM and SRM are combined to define the RPM for predicting the thermo-ablative
¹⁸² response of the TPS under hypersonic boundary layers. Specifically, the RPM is defined as
¹⁸³ the LCM as in eq. (9), where the *geometry- and temperature-dependent matrices* $\tilde{\mathbf{A}}$, $\tilde{\mathbf{B}}$, and
¹⁸⁴ $\tilde{\mathbf{f}}$ are updated at each time step based on the current temperature $\bar{\mathbf{u}}$ and displacements \mathbf{w}
¹⁸⁵ provided by the SRM. The RPM is formally stated as,

$$\tilde{\mathbf{A}}(\mathbf{s})\dot{\mathbf{s}} = \tilde{\mathbf{B}}(\mathbf{s})\mathbf{s} + \tilde{\mathbf{F}}(t) \quad (14a)$$

$$\tilde{\mathbf{z}} = \mathbf{I}\mathbf{s} \quad (14b)$$

¹⁸⁶ where the state $\mathbf{s} = [\bar{\mathbf{u}}, \mathbf{w}]^\top \in \mathbb{R}^{N+\tilde{N}}$ includes the *average temperature* and *one-dimensional*
¹⁸⁷ *surface displacements*, and \tilde{N} is the number of ablating components with $\tilde{N} \leq N$. Moreover,
¹⁸⁸ the observables are defined as $\mathbf{z} = [\bar{\mathbf{u}}, \mathbf{w}]^\top \in \mathbb{R}^{N+\tilde{N}}$. The matrices are given as,

$$\tilde{\mathbf{A}}(\mathbf{s}) = \begin{bmatrix} \bar{\mathbf{A}}(\mathbf{s}) & \mathbf{0} \\ \mathbf{0} & \mathbf{I} \end{bmatrix}, \quad \tilde{\mathbf{B}}(\mathbf{s}) = \begin{bmatrix} \bar{\mathbf{B}}(\mathbf{s}) & \mathbf{0} \\ \boldsymbol{\Xi} & \mathbf{0} \end{bmatrix}, \quad \tilde{\mathbf{F}}(t) = \begin{bmatrix} \bar{\mathbf{f}}(t) \\ -\tilde{\mathbf{f}} \end{bmatrix} \quad (15)$$

¹⁸⁹ In the matrices $\tilde{\mathbf{A}}$ and $\tilde{\mathbf{B}}$, the surface displacements \mathbf{w} are used to define the dimensions for
¹⁹⁰ the Ω_i component used in eqs. (11) and (12), thus effectively coupling the LCM and SRM.

191 2.4 Summary of Modeling Approaches

192 The FOM (i.e., FEM) and RPM (i.e., LCM with SRM) are two different but mathemati-
193 cally connected solution strategies. Particularly, the LCM in eq. (9) not only resembles the
194 functional form of the DG model in eq. (8), but can be viewed as a special case of the latter,
195 where the mesh partition is extremely coarse, and the trial and test functions are piece-wise
196 constants. This removes all spatial variations within each component, and neglects advection
197 effects due to mesh motion.

198 For example, consider the case where each component Ω_i is treated as one single element,
199 and each element employs one constant basis function $\phi_i = 1$. The element-wise DG model
200 in eq. (7) simplifies into a scalar ODE,

$$\mathbf{A}^{(i)} = \bar{A}_i, \quad \mathbf{C}^{(i)} = 0, \quad \mathbf{B}_{ij}^{(i)} = -\sigma|e_{ij}|, \quad \mathbf{B}_{ij}^{(j)} = \sigma|e_{ij}|, \quad \mathbf{f}_i = |e_{iq}|\bar{q}_i + \sigma|e_{iT}|\bar{T}_i \quad (16)$$

201 Clearly, the LCM is a coarse zeroth-order DG model with the inverse of thermal resistance
202 chosen as the element-wise penalty factors. Or conversely, the DG model is a refined version
203 of LCM via *hp*-adaptation.

204 The FOM and RPM represent two extremes in the modeling fidelity and computational
205 cost spectrum. On one hand, the FOM is the most accurate but computationally expensive
206 to evaluate due to the fine mesh discretizations for both the temperature and displacement
207 fields, leading to possibly millions of state variables. On the other hand, the RPM consid-
208 ers only the average temperature of the material, from which the one-dimensional surface
209 displacements are computed by integrating eq. (13). This considerably reduces the com-
210 putational cost, but sacrifices local temperature information that are critical to properly
211 capture higher-order effects due to mesh motion and thermal gradients within each compo-
212 nent. Thus, neither the FOM nor the RPM is an universal approach for real-world analysis,
213 design, and optimization tasks for ablating TPS, where thousands of high-fidelity model
214 evaluations may be necessary. This issue motivates the development of the PIROM, which
215 can achieve the fidelity of FOM at a computational cost close to the RPM, while maintaining
216 the generalizability to model parameters.

217 3 Physics-Infused Reduced-Order Modeling

218 The formulation of PIROM for ablating TPS starts by connecting the FOM, i.e., the DG-
219 FEM, and the RPM, i.e., the LCM, via a coarse-graining procedure. This procedure pin-
220 points the missing dynamics in the LCM when compared to DG-FEM. Subsequently, the
221 Mori-Zwanzig (MZ) formalism is employed to determine the model form for the missing dy-
222 namics in PIROM. Lastly, the data-driven identification of the missing dynamics in PIROM
223 is presented.

224 3.1 Deriving the Reduced-Physics Model via Coarse-Graining

225 The subsequent coarse-graining formulation is performed on the DG-FEM in eq. (8) to derive
226 the LCM in eq. (9). This process constraints the trial function space of a full-order DG model
227 to a subset of piece-wise constants, so that the variables \mathbf{u} , matrices \mathbf{A} , \mathbf{B} , and \mathbf{C} , and forcing

228 vector \mathbf{f} are all approximated using a single state associated to the average temperature.
229 Note that the coarse-graining is exclusively performed on the thermal dynamics, as it is
230 the surface temperature that drives the one-dimensional recession via the SRM. Hence, the
231 coarse-graining of the mesh dynamics is not included in the following procedure.

232 3.1.1 Coarse-Graining of States

233 Consider a DG model as in eq. (8) for M elements and an LCM as in eq. (9) for N components;
234 clearly $M \gg N$. Let $\mathcal{V}_j = \{i | E_i \in \Omega_j\}$ be the indices of the elements belonging to the j -th
235 component, so $E_i \in \Omega_j$ for all $i \in \mathcal{V}_j$. The number of elements in the j -th component is $|\mathcal{V}_j|$.
236 The average temperature on Ω_j is,

$$\bar{u}_j = \frac{1}{|\Omega_j|} \sum_{i \in \mathcal{V}_j} \int_{E^{(i)}} \boldsymbol{\phi}^{(i)}(x)^T \mathbf{u}^{(i)} d\Omega = \frac{1}{|\Omega_j|} \sum_{i \in \mathcal{V}_j} |E_i| \boldsymbol{\varphi}_i^{j\top} \mathbf{u}^{(i)}, \quad j = 1, 2, \dots, N \quad (17)$$

237 where $|\Omega_j|$ and $|E_i|$ denote the area ($d = 2$) or volume ($d = 3$) of component j and element
238 i , respectively. The orthogonal basis functions are defined as $\boldsymbol{\varphi}_i^{j\top} = [1, 0, \dots, 0]^\top \in \mathbb{R}^P$.

239 Conversely, given the average temperatures of the N components, $\bar{\mathbf{u}}$, the states of an
240 arbitrary element E_i is written as,

$$\mathbf{u}^{(i)} = \sum_{k=1}^N \boldsymbol{\varphi}_i^k \bar{u}_k + \delta \mathbf{u}^{(i)}, \quad i = 1, 2, \dots, M \quad (18)$$

241 where $\boldsymbol{\varphi}_i^k = 0$ if $i \notin \mathcal{V}_k$, and $\delta \mathbf{u}^{(i)}$ represents the deviation from the average temperature and
242 satisfies the orthogonality condition $\boldsymbol{\varphi}_i^{k\top} \delta \mathbf{u}^{(i)} = 0$ for all k .

243 Equations eqs. (17) and (18) are combined and written in matrix form as,

$$\bar{\mathbf{u}} = \boldsymbol{\Phi}^+ \mathbf{u}, \quad \mathbf{u} = \boldsymbol{\Phi} \mathbf{u} + \delta \mathbf{u} \quad (19)$$

244 where $\boldsymbol{\Phi} \in \mathbb{R}^{MP \times N}$ is a matrix of $M \times N$ blocks, with the (i, j) -th block as $\boldsymbol{\varphi}_i^j$, $\boldsymbol{\Phi}^+ \in \mathbb{R}^{N \times MP}$
245 is the left inverse of $\boldsymbol{\Phi}$, with the (i, j) -th block as $\boldsymbol{\varphi}_i^{j+} = \frac{|E_i|}{|\Omega_j|} \boldsymbol{\varphi}_i^{j\top}$, and $\delta \mathbf{u}$ is the collection of
246 deviations. By their definitions, $\boldsymbol{\Phi}^+ \boldsymbol{\Phi} = \mathbf{I}$ and $\boldsymbol{\Phi}^+ \delta \mathbf{u} = \mathbf{0}$.

247 3.1.2 Coarse-Graining of Dynamics

248 The dependence of the matrices with respect to the displacements \mathbf{w} is dropped to isolate
249 the analysis based on coarsened variables. Consider a function of states in the form of
250 $\mathbf{M}(\mathbf{u}) \mathbf{g}(\mathbf{u})$, where $\mathbf{g} : \mathbb{R}^{MP} \rightarrow \mathbb{R}^{MP}$ is a vector-valued function, and $\mathbf{M} : \mathbb{R}^{MP} \rightarrow \mathbb{R}^{p \times MP}$
251 is a matrix-valued function with an arbitrary dimension p . Define the projection matrix
252 $\mathbf{P} = \boldsymbol{\Phi} \boldsymbol{\Phi}^+$ and the projection operator \mathcal{P} as,

$$\begin{aligned} \mathcal{P} [\mathbf{M}(\mathbf{u}) \mathbf{g}(\mathbf{u})] &= \mathbf{M}(\mathbf{P} \mathbf{u}) \mathbf{g}(\mathbf{P} \mathbf{u}) \\ &= \mathbf{M}(\boldsymbol{\Phi} \bar{\mathbf{u}}) \mathbf{g}(\boldsymbol{\Phi} \bar{\mathbf{u}}) \end{aligned} \quad (20)$$

so that the resulting function depends only on the average temperatures $\bar{\mathbf{u}}$. Correspondingly, the residual operator $\mathcal{Q} = \mathcal{I} - \mathcal{P}$, and $\mathcal{Q}[\mathbf{M}(\mathbf{u})\mathbf{g}(\mathbf{u})] = \mathbf{M}(\mathbf{u})\mathbf{g}(\mathbf{u}) - \mathbf{M}(\Phi\bar{\mathbf{u}})\mathbf{g}(\Phi\bar{\mathbf{u}})$. When the function is not separable, the projection operator is simply defined as $\mathcal{P}[\mathbf{g}(\mathbf{u})] = \mathbf{g}(\mathbf{P}\mathbf{u})$.

Subsequently, the operators defined above are applied to coarse-grain the dynamics. First, write the DG-FEM in eq. (8) as,

$$\dot{\mathbf{u}} = \mathbf{A}(\mathbf{u})^{-1}\mathbf{B}(\mathbf{u})\mathbf{u} + \mathbf{A}(\mathbf{u})^{-1}\mathbf{C}(\mathbf{u})\mathbf{u} + \mathbf{A}(\mathbf{u})^{-1}\mathbf{f}(t) \quad (21)$$

and multiply both sides by Φ^+ to obtain,

$$\Phi^+\dot{\mathbf{u}} = \Phi^+(\Phi\dot{\mathbf{u}} + \delta\dot{\mathbf{u}}) = \dot{\mathbf{u}} = \Phi^+\mathbf{r}(\mathbf{u}, t) \quad (22)$$

Apply the projection operator \mathcal{P} and the residual operator \mathcal{Q} to the right-hand side to obtain,

$$\dot{\mathbf{u}} = \mathcal{P}[\Phi^+\mathbf{r}(\mathbf{u}, t)] + \mathcal{Q}[\Phi^+\mathbf{r}(\mathbf{u}, t)] \equiv \mathbf{r}^{(1)}(\mathbf{u}, t) + \mathbf{r}^{(2)}(\mathbf{u}, t) \quad (23)$$

where $\mathbf{r}^{(1)}(\mathbf{u}, t)$ is resolved dynamics that depends on $\bar{\mathbf{u}}$ only, and $\mathbf{r}^{(2)}(\mathbf{u}, t)$ is the un-resolved or residual dynamics. Detailed derivations and analysis of $\mathbf{r}^{(1)}(\mathbf{u}, t)$ and $\mathbf{r}^{(2)}(\mathbf{u}, t)$ can be found in the Appendix.

It follows from Ref. [13] that the resolved dynamics is exactly the LCM, where the advection term reduces to zero, i.e., $\bar{\mathbf{C}}(\bar{\mathbf{u}}) = \mathbf{0}$ as shown in the Appendix. Using the notation from eq. (9), it follows that,

$$\begin{aligned} \mathbf{r}^{(1)}(\mathbf{u}, t) &= \bar{\mathbf{A}}(\bar{\mathbf{u}})^{-1}\bar{\mathbf{B}}(\bar{\mathbf{u}})\bar{\mathbf{u}} + \bar{\mathbf{A}}(\bar{\mathbf{u}})^{-1}\bar{\mathbf{C}}(\bar{\mathbf{u}})\bar{\mathbf{u}} + \bar{\mathbf{A}}(\bar{\mathbf{u}})^{-1}\bar{\mathbf{f}}(\bar{\mathbf{u}}) \\ &= \bar{\mathbf{A}}(\bar{\mathbf{u}})^{-1}\bar{\mathbf{B}}(\bar{\mathbf{u}})\bar{\mathbf{u}} + \bar{\mathbf{A}}(\bar{\mathbf{u}})^{-1}\bar{\mathbf{f}}(t) \end{aligned} \quad (24)$$

where the following relations hold,

$$\bar{\mathbf{A}}(\bar{\mathbf{u}}) = \mathbf{W}(\Phi^+\mathbf{A}(\Phi\bar{\mathbf{u}})^{-1}\Phi)^{-1} \quad (25a)$$

$$\bar{\mathbf{B}}(\bar{\mathbf{u}}) = \mathbf{W}\Phi^+\mathbf{B}(\Phi\bar{\mathbf{u}})\Phi \quad (25b)$$

where $\mathbf{W} \in \mathbb{R}^{N \times N}$ is a diagonal matrix with the i -th element as $[\mathbf{W}]_{ii} = |\mathcal{V}_k|$ if $i \in \mathcal{V}_k$. The examination of the second residual term $\mathbf{r}^{(2)}(\mathbf{u}, t)$ in eq. (23) is shown in the Appendix, and demonstrates that the physical sources of missing dynamics in the LCM include: the approximation of non-uniform temperature within each component as a constant, and the elimination of the advection term due to coarse-graining. In sum, the above results not only show that the LCM is a result of coarse-graining of the full-order DG-FEM, but also reveal the discrepancies between the LCM and the DG-FEM. These discrepancies propagate into the SRM, which as a result of the averaging in the LCM formulation, under-predicts the surface recession rates. In the subsequent section, the discrepancies in the LCM are corrected to formulate the PIROM.

3.2 Physics-Infusion Via Mori-Zwanzig Formalism

The Mori-Zwanzig (MZ) formalism is an operator-projection technique used to derive ROMs for high-dimensional dynamical systems, especially in statistical mechanics and fluid dy-

namics [10, 11, 12]. It provides an exact reformulation of a high-dimensional Markovian dynamical system, into a low-dimensional observable non-Markovian dynamical system. The proposed ROM is subsequently developed based on the approximation to the non-Markovian term in the observable dynamics. Particularly, eq. (23) shows that the DG-FEM dynamics can be decomposed into the resolved dynamics $\mathbf{r}^{(1)}(\mathbf{u}, t)$ and the orthogonal dynamics $\mathbf{r}^{(2)}(\mathbf{u}, t)$, in the sense of $\mathcal{P}\mathbf{r}^{(2)} = 0$. In this case, the MZ formalism can be invoked to express the dynamics $\bar{\mathbf{u}}$ in terms of $\bar{\mathbf{u}}$ alone as the projected Generalized Langevin Equation (GLE) [10, 11, 12],

$$\dot{\bar{\mathbf{u}}}(t) = \mathbf{r}^{(1)}(\bar{\mathbf{u}}, t) + \int_0^t \tilde{\boldsymbol{\kappa}}(t, s, \bar{\mathbf{u}}) ds \quad (26)$$

where the first and second terms are referred to as the Markovian and non-Markovian terms, respectively. The non-Markovian term accounts for the effects of past un-resolved states on the current resolved states via a memory kernel $\tilde{\boldsymbol{\kappa}}(t, s, \bar{\mathbf{u}})$, which in practice is computationally expensive to evaluate.

3.2.1 Markovian Reformulation

This section details the formal derivation of the PIROM as a system of ODEs for the thermal dynamics, based on approximations to the memory kernel. Specifically, the kernel $\tilde{\boldsymbol{\kappa}}$ is examined via a leading-order expansion, based on prior work [14]; this can be viewed as an analog of zeroth-order holding in linear system theory with a sufficiently small time step. In this case, the memory kernel is approximated as,

$$\tilde{\boldsymbol{\kappa}}(t, s, \bar{\mathbf{u}}) \approx \mathbf{r}^{(1)}(\bar{\mathbf{u}}, t) \cdot \nabla_{\bar{\mathbf{u}}} \mathbf{r}^{(2)}(\Phi \bar{\mathbf{u}}, t) \quad (27)$$

Note that the terms in $\mathbf{r}^{(1)}$ have a common factor $\bar{\mathbf{A}}^{-1}$; this motivates the following heuristic modification of the model form in eq. (26),

$$\dot{\bar{\mathbf{u}}} = \mathbf{r}^{(1)}(\bar{\mathbf{u}}, t) + \bar{\mathbf{A}}^{-1}(\bar{\mathbf{u}}) \int_0^t \boldsymbol{\kappa}(t, s, \bar{\mathbf{u}}) ds \quad (28a)$$

$$\bar{\mathbf{A}}(\bar{\mathbf{u}}) \dot{\bar{\mathbf{u}}} = \bar{\mathbf{B}}(\bar{\mathbf{u}}) \bar{\mathbf{u}} + \bar{\mathbf{f}}(t) + \int_0^t \boldsymbol{\kappa}(t, s, \bar{\mathbf{u}}) ds \quad (28b)$$

where the original kernel $\tilde{\boldsymbol{\kappa}}$ is effectively normalized by $\bar{\mathbf{A}}^{-1}$. Intuitively, such choice of kernel reduces its dependency on the averaged material properties, and simplifies the subsequent design of model form.

Subsequently, the hidden states are introduced to “Markovianize” the system eq. (26). In this manner, eq. (28b) is converted into a pure state-space model, with the functional form of the LCM retained; since LCM is a physics-based model, then it encodes the physical information and retains explicit parametric dependence of the problem. Consider the representation of the kernel as a finite sum of simpler functions, e.g., exponentials,

$$\boldsymbol{\kappa}(t, s, \bar{\mathbf{u}}) = \sum_{j=1}^m \mathcal{K}_j(t, s, \bar{\mathbf{u}}) [\mathbf{p}_j + \mathbf{d}_j(\bar{\mathbf{u}})] \phi_j(s, \bar{\mathbf{u}}) \quad (29)$$

308 where,

$$\mathcal{K}_j(t, s, \bar{\mathbf{u}}) = e^{-\int_s^t (\lambda_j + e_j(\bar{\mathbf{u}})) d\tau}, \quad \phi_j(s, \bar{\mathbf{u}}) = \mathbf{q}_j^\top \bar{\mathbf{u}}(s) + \mathbf{g}_j(\bar{\mathbf{u}})^\top \bar{\mathbf{u}}(s) + \mathbf{r}_j^\top \bar{\mathbf{f}}(s) \quad (30)$$

309 with suitable coefficients $\mathbf{p}_j, \mathbf{d}_j, \mathbf{q}_j, \mathbf{g}_j, \mathbf{r}_j \in \mathbb{R}^N$ and decay rates $\lambda_j, e_j(\bar{\mathbf{u}}) > 0$, that need to
310 be identified from data.

311 Define the hidden states as,

$$\beta_j(t) = \int_0^t \mathcal{K}_j(s, \bar{\mathbf{u}}) \phi_j(s, \bar{\mathbf{u}}) ds \quad (31)$$

312 and differentiate with respect to time,,

$$\dot{\beta}_j(t) = -[\lambda_j + e_j(\bar{\mathbf{u}})] \beta_j(t) + \mathbf{q}_j^\top \bar{\mathbf{u}}(t) + \mathbf{g}_j(\bar{\mathbf{u}})^\top \bar{\mathbf{u}}(t) + \mathbf{r}_j^\top \bar{\mathbf{f}}(t) \quad (32)$$

313 to obtain the memory,

$$\int_0^t \boldsymbol{\kappa}(t, s, \bar{\mathbf{u}}) ds = \sum_{j=1}^m [\mathbf{p}_j + \mathbf{d}_j(\bar{\mathbf{u}})] \beta_j(t) \quad (33)$$

314 Then, eq. (28b) is recast as the extended Markovian system,

$$\bar{\mathbf{A}}(\bar{\mathbf{u}}) \dot{\bar{\mathbf{u}}} = \bar{\mathbf{B}}(\bar{\mathbf{u}}) \bar{\mathbf{u}} + [\mathbf{P} + \mathbf{D}(\bar{\mathbf{u}})] \boldsymbol{\beta} + \bar{\mathbf{f}}(t) \quad (34a)$$

$$\dot{\boldsymbol{\beta}} = [\mathbf{Q} + \mathbf{G}(\bar{\mathbf{u}})] \bar{\mathbf{u}} + [\mathbf{E}(\bar{\mathbf{u}}) - \boldsymbol{\Lambda}] \boldsymbol{\beta} + \mathbf{R} \bar{\mathbf{f}}(t) \quad (34b)$$

315 where the data-driven operators associated to the hidden dynamics are collected as,

$$\boldsymbol{\Lambda} = \text{diag}(\lambda_1, \lambda_2, \dots, \lambda_m) \in \mathbb{R}^{m \times m}, \quad \mathbf{P} = [\mathbf{p}_1, \mathbf{p}_2, \dots, \mathbf{p}_m] \in \mathbb{R}^{N \times m} \quad (35a)$$

$$\mathbf{D}(\bar{\mathbf{u}}) = [\mathbf{d}_1(\bar{\mathbf{u}}), \mathbf{d}_2(\bar{\mathbf{u}}), \dots, \mathbf{d}_m(\bar{\mathbf{u}})] \in \mathbb{R}^{N \times m}, \quad \mathbf{Q} = [\mathbf{q}_1, \mathbf{q}_2, \dots, \mathbf{q}_m] \in \mathbb{R}^{m \times N} \quad (35b)$$

$$\mathbf{G}(\bar{\mathbf{u}}) = [\mathbf{g}_1(\bar{\mathbf{u}}), \mathbf{g}_2(\bar{\mathbf{u}}), \dots, \mathbf{g}_m(\bar{\mathbf{u}})] \in \mathbb{R}^{m \times N}, \quad \mathbf{R} = [\mathbf{r}_1, \mathbf{r}_2, \dots, \mathbf{r}_m] \in \mathbb{R}^{m \times N} \quad (35c)$$

$$\mathbf{E}(\bar{\mathbf{u}}) = \text{diag}(e_1(\bar{\mathbf{u}}), e_2(\bar{\mathbf{u}}), \dots, e_m(\bar{\mathbf{u}})) \in \mathbb{R}^{m \times m} \quad (35d)$$

316 The form of the temperature-dependent matrices $\mathbf{D}(\bar{\mathbf{u}})$, $\mathbf{G}(\bar{\mathbf{u}})$, and $\mathbf{E}(\bar{\mathbf{u}})$ is specified in the
317 next section. Since the hidden states $\boldsymbol{\beta}$ serve as the memory, their initial conditions are set
318 to zero, i.e., $\boldsymbol{\beta}(t_0) = \mathbf{0}$, no memory at the beginning. The physics-infused model in eq. (34)
319 retains the structure of the LCM, while the hidden states account for missing physics through
320 corrections to the stiffness and advection matrices, as well as the forcing term.

321 3.2.2 Coupled Physics-Infused Model

322 The next step involves coupling the physics-infused model in eq. (34) with the SRM in
323 eq. (13) to define the PIROM for ablating TPS. To this end, define the observables as the
324 surface temperature $\mathbf{z}_u \in \mathbb{R}^{\tilde{N}}$ and displacements $\mathbf{z}_w \in \mathbb{R}^{\tilde{N}}$ for $\tilde{N} \leq N$ ablating components
325 to define the observable vector as $\mathbf{z} = [\mathbf{z}_u, \mathbf{z}_w]^\top \in \mathbb{R}^{n_z}$ with $n_z = 2\tilde{N}$ as the total number of
326 observables.

327 Collect the RPM and hidden states into a single state vector $\mathbf{y} = [\bar{\mathbf{u}}, \mathbf{w}, \boldsymbol{\beta}]^\top \in \mathbb{R}^{n_y}$, where
 328 $n_y = N + \tilde{N} + m$, and define a data-driven operator $\mathbf{M} \in \mathbb{R}^{n_z \times n_y}$ to define the PIROM's
 329 observable as,

$$\mathbf{z} = \mathbf{My} \quad (36)$$

330 where,

$$\mathbf{M} = \begin{bmatrix} \mathbf{M}_{\bar{u}} & \mathbf{0} & \mathbf{M}_\beta \\ \mathbf{0} & \mathbf{I} & \mathbf{0} \end{bmatrix} \quad (37)$$

331 includes the matrices $\mathbf{M}_{\bar{u}} \in \mathbb{R}^{\tilde{N} \times N}$ and $\mathbf{M}_\beta \in \mathbb{R}^{\tilde{N} \times m}$, which computes the surface tempera-
 332 ture observable from the RPM states and hidden states, respectively. The PIROM is coupled
 333 to the SRM in eq. (13) by leveraging eq. (36) to compute the surface recession velocity. Thus,
 334 the PIROM is formally stated as,

$$\mathcal{A}\dot{\mathbf{y}} = [\mathcal{B} + \mathcal{C}]\mathbf{y} + \mathcal{F}(t) \quad (38a)$$

$$\mathbf{z} = \mathbf{My} \quad (38b)$$

335 where,

$$\mathcal{A} = \begin{bmatrix} \bar{\mathbf{A}} & \mathbf{O} & \mathbf{O} \\ \mathbf{O} & \mathbf{I} & \mathbf{O} \\ \mathbf{O} & \mathbf{O} & \mathbf{I} \end{bmatrix} \in \mathbb{R}^{n_y \times n_y}, \quad \mathcal{B} = \begin{bmatrix} \bar{\mathbf{B}} & \mathbf{O} & \mathbf{P} \\ \Xi\mathbf{M}_u & \mathbf{O} & \Xi\mathbf{M}_\beta \\ \mathbf{Q} & \mathbf{O} & -\Lambda \end{bmatrix} \in \mathbb{R}^{n_y \times n_y}, \quad (39a)$$

$$\mathcal{C} = \begin{bmatrix} \mathbf{O} & \mathbf{O} & \mathbf{D}(\bar{\mathbf{u}}) \\ \mathbf{O} & \mathbf{O} & \mathbf{O} \\ \mathbf{G}(\bar{\mathbf{u}}) & \mathbf{O} & \mathbf{E}(\bar{\mathbf{u}}) \end{bmatrix} \in \mathbb{R}^{n_y \times n_y}, \quad \mathcal{F} = \begin{bmatrix} \bar{\mathbf{f}}(t) \\ -\tilde{\mathbf{f}} \\ \mathbf{R}\bar{\mathbf{f}}(t) \end{bmatrix} \in \mathbb{R}^{n_y} \quad (39b)$$

336 The learnable parameters in the PIROM are collected as,

$$\Theta = \{\mathbf{P}, \mathbf{Q}, \mathbf{R}, \mathbf{D}(\bar{\mathbf{u}}), \mathbf{G}(\bar{\mathbf{u}}), \mathbf{E}(\bar{\mathbf{u}}), \mathbf{M}_u, \mathbf{M}_\beta\}, \in \mathbb{R}^{n_\theta} \quad (40)$$

337 Particularly, the matrices $\mathbf{P}, \Lambda, \mathbf{Q}, \mathbf{R}$ are constants that need to be identified from data, and
 338 account for the effects of coarse-graining on the stiffness and forcing matrices. The matrices
 339 $\mathbf{D}(\bar{\mathbf{u}}), \mathbf{E}(\bar{\mathbf{u}}), \mathbf{G}(\bar{\mathbf{u}})$ are state-dependent matrices, and account for the effects of coarse-graining
 340 on the advection matrix due to mesh motion. Leveraging the DG-FEM formula for the
 341 advection matrix in eq. (55c) in the Appendix, and noting that the ablating velocity in
 342 eq. (4) imposes the boundary condition for the mesh motion, the state-dependent matrices
 343 for the i -th component are written as,

$$\mathbf{D}(\bar{\mathbf{u}}) \approx \dot{\mathbf{w}}(\bar{\mathbf{u}}) \odot_r \mathbf{D}, \quad \mathbf{G}(\bar{\mathbf{u}}) \approx \mathbf{G} \odot_r \dot{\mathbf{w}}(\bar{\mathbf{u}}), \quad \mathbf{E}(\bar{\mathbf{u}}) \approx \dot{\mathbf{W}}(\bar{\mathbf{u}}) \odot \mathbf{E} \quad (41)$$

344 where $\dot{\mathbf{w}}(\bar{\mathbf{u}})$ is the SRM based on the observable temperature $\bar{\mathbf{u}}$, \odot_r is the row-wise multipli-
 345 cation, and $\dot{\mathbf{W}}$ is the concatenation of $\dot{\mathbf{w}}$ for \tilde{m} times, where \tilde{m} corresponds to the number
 346 of hidden states per component, i.e., $m = N\tilde{m}$.

347 The PIROM in eq. (38) incorporates explicit information on the material properties,
 348 boundary conditions, and surface recession, and is designed to generalize across parametric
 349 variations in these inputs. Moreover, the hidden dynamics in eq. (34) are interpretable, as

³⁵⁰ these retain the functional form of the DG-FEM in eq. (8). The next step is focused on
³⁵¹ identifying the unknown data-driven parameters Θ characterizing the hidden dynamics.

³⁵² 3.3 Learning the Hidden Dynamics

³⁵³ Learning of the PIROM is achieved through a gradient-based neural-ODE-like approach [3].
³⁵⁴ For ease of presentation, consider the compact form of the PIROM in eq. (38),

$$\mathcal{D}(\dot{\mathbf{y}}, \mathbf{y}, \boldsymbol{\xi}, \mathcal{F}; \Theta) = \mathbf{0} \quad (42)$$

³⁵⁵ where $\boldsymbol{\xi}$ defines the model parameters, i.e., material properties and B' tables, while \mathcal{F}
³⁵⁶ represents the forcing terms, i.e., the boundary conditions.

³⁵⁷ Consider a dataset of N_s high-fidelity *surface temperature* observable trajectories \mathbf{z}_{HF} ,
³⁵⁸ sampled at p time instances $\{t_k\}_{k=0}^{p-1}$, for different parameter settings $\{\boldsymbol{\xi}^{(l)}\}_{l=1}^{N_s}$ and forcing
³⁵⁹ functions $\{\mathcal{F}^{(l)}(t)\}_{l=1}^{N_s}$. The dataset is expressed as,

$$\mathcal{D} = \left\{ \left(t_k, \mathbf{z}_{\text{HF}}^{(l)}(t_k), \boldsymbol{\xi}^{(l)}, \mathcal{F}^{(l)}(t_k) \right) \right\}_{l=1}^{N_s}, \quad k = 0, 1, \dots, p-1 \quad (43)$$

³⁶⁰ In this work, the dataset contains only surface temperature observables – all high-fidelity
³⁶¹ information regarding the surface displacements *are assumed to be unavailable during learning*.

³⁶³ The learning problem is formulated as the following differentially-constrained problem,

$$\min_{\Theta} \mathcal{J}(\Theta; \mathcal{D}) = \sum_{l=1}^{N_s} \int_{t_0}^{t_f} \ell \left(\mathbf{z}_u^{(l)}, \mathbf{z}_{\text{HF}}^{(l)} \right) dt \quad (44a)$$

$$\text{s.t. } \mathbf{0} = \mathcal{D} \left(\dot{\mathbf{y}}^{(l)}, \mathbf{y}^{(l)}, \boldsymbol{\xi}^{(l)}, \mathcal{F}^{(l)}; \Theta \right) \quad (44b)$$

³⁶⁴ for $l = 1, 2, \dots, N_s$, the objective is to minimize the discrepancy between the high-fidelity
³⁶⁵ and PIROM predictions for the l -th trajectory with $\ell \left(\mathbf{z}_u^{(l)}, \mathbf{z}_{\text{HF}}^{(l)} \right) = \left\| \mathbf{z}_u^{(l)} - \mathbf{z}_{\text{HF}}^{(l)} \right\|_2^2$.

³⁶⁶ The gradient-based optimization loop is based on the adjoint variable $\boldsymbol{\lambda}$, governed by the
³⁶⁷ adjoint differential equation,

$$\frac{\partial \ell}{\partial \mathbf{y}} + \boldsymbol{\lambda}^\top \frac{\partial \mathcal{D}}{\partial \mathbf{y}} - \frac{d}{dt} \left(\boldsymbol{\lambda}^\top \frac{\partial \mathcal{D}}{\partial \dot{\mathbf{y}}} \right) = \mathbf{0} \quad (45a)$$

$$\boldsymbol{\lambda}(t_f)^\top \frac{\partial \mathcal{D}}{\partial \dot{\mathbf{y}}(t_f)} = \mathbf{0} \quad (45b)$$

³⁶⁸ Once $\boldsymbol{\lambda}$ is solved, the gradient is computed as,

$$\nabla_{\Theta} \mathcal{J} = \frac{1}{N_s} \sum_{l=1}^{N_s} \int_{t_0}^{t_f} \left(\frac{\partial \ell}{\partial \Theta} + \left(\boldsymbol{\lambda}^{(l)} \right)^\top \frac{\partial \mathcal{D}}{\partial \Theta} \right) dt \quad (46)$$

Component	w (cm)	h (cm)	ρ (kg/m ³)	c_p (J/kg·K)	k (W/m·K)	$\alpha \times 10^{-6}$ (m/s·K)
#1	0.3	0.03	160	1200	0.2	1
#2	0.3	0.03	1800	900	5	1
#3	0.3	0.03	300	1500	0.15	1
#4	0.9	0.03	1600	800	10	0

Table 1: Description of TPS components, including thickness h , density ρ , specific heat capacity c_p , thermal conductivity k , and SRM parameter α .

369 4 Application to Thermal Protection Systems

370 In this section, the proposed PIROM approach is applied to the analysis of thermo-ablative
 371 multi-layered hypersonic TPS. The performance of the PIROM is evaluated in terms of the
 372 three corners of the ITM in Fig. x, across a wide range of boundary condition and SRM
 373 model parametrizations. The results show PIROM to be a promising candidate for the
 374 solution of the impossible trinity of modeling.

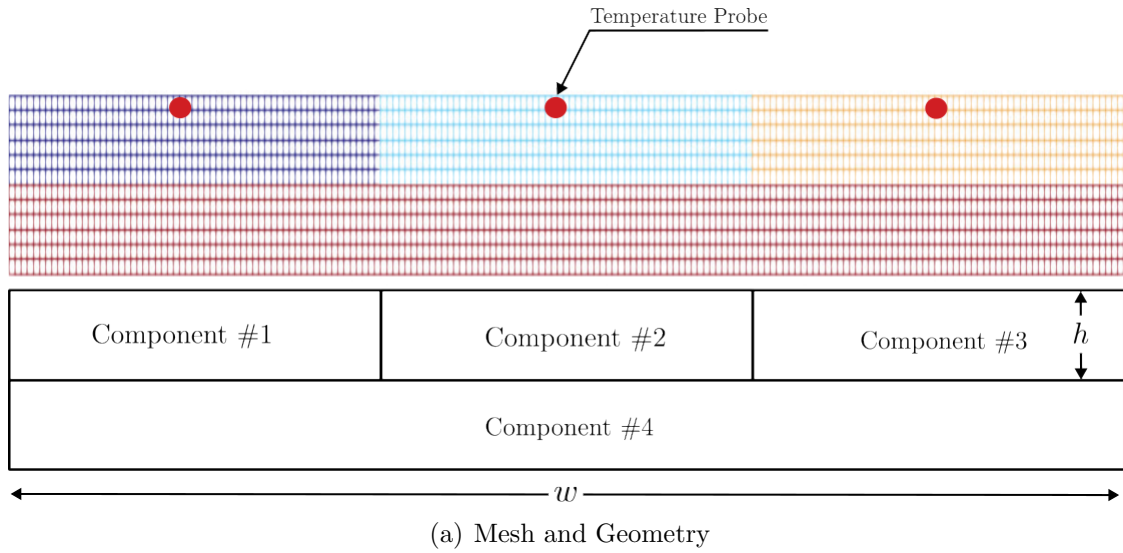
375 4.1 Problem Definition

376 Consider the two-dimensional TPS configuration shown in Fig. 2 with constant material
 377 properties within each layer, dimensions, and BCs listed in Table 1. Such configuration is
 378 representative of the TPS used for the initial concept 3.X vehicle in past studies [8], and in-
 379 volves two main layers: an outer ablative layer, and an inner substrate layer. The top ablative
 380 layer may be composed of different materials, such as PICA or Avcoat, while the substrate
 381 layer is typically made of a high-temperature resistant material, such as carbon-carbon com-
 382 posite [6]. The ablative layer, composed of $\tilde{N} = 3$ ablative components, is subjected to
 383 strong time-varying and non-uniform heating, while the substrate layer, composed of one
 384 non-ablative component, is insulated adiabatically at the outer surface; the total number of
 385 components is thus $N = 4$.

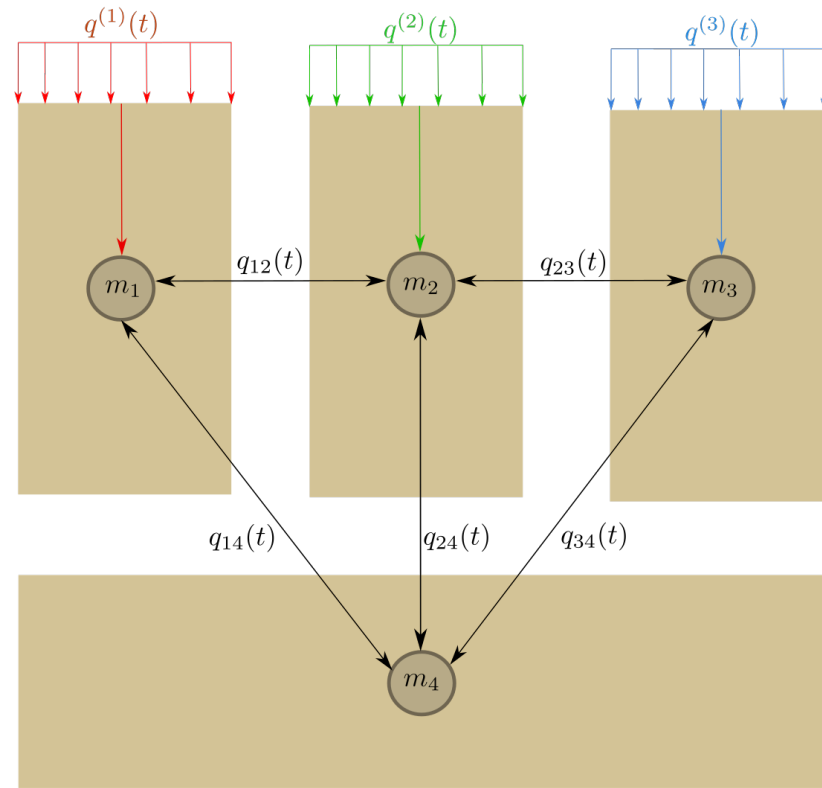
386 The lumped-mass representation of the TPS configuration is shown in Fig. 2(b), where
 387 each component Ω_i is represented by a lumped mass with uniform temperature $u_i(t)$. Details
 388 regarding the derivation of the LCM for this configuration are provided in Appendix A.
 389 The sources of non-linearities studied in this problem originate from the coupling between
 390 the thermodynamics and temperature-dependent mesh motion, i.e., geometry-dependent
 391 matrices, as well as the heterogeneities across material layers. As shown in Fig. 2, perfect
 392 thermocouple devices are placed at the surfaces of the ablative layers for the collection of
 393 the high-fidelity temperature signals that are used in the following sections for training and
 394 testing the PIROM.

395 4.2 Problem Parametrization

396 The operating conditions of the TPS are specified by the boundary conditions, i.e., the heat
 397 flux, and the surface recession model (SRM). Specifically, the heat flux on the Neumann
 398 BC is parametrized using $\xi_{BC} = \{\xi_0, \xi_1, \xi_2\}$, while the SRM is parametrized using $\xi_{SRM} =$
 399 $\{\alpha_1, \alpha_2, \alpha_3\}$. Thus, the heat flux and SRM over the i -th ablative component are expressed



(a) Mesh and Geometry



(b) Lumped Mass Representation

Figure 2: Four-component TPS geometry and lumped-mass representation for the TPS.

400 as,

$$q(x, t; \boldsymbol{\xi}_{\text{BC}}) = \xi_0 e^{\xi_1 x} e^{\xi_2 t}, \forall x \in \Gamma_{i,q}, \quad \dot{w}_i(z_{u,i}; \boldsymbol{\xi}_{\text{SRM}}) = \alpha_i (z_{u,i} - u_{0,i}) \quad (47)$$

401 where $\Gamma_{i,q}$, $z_{u,i}$, and $u_{0,i}$ correspond to the Neumann BC surface, the PIROM's surface tem-
402 perature prediction, and the initial temperature of the i -th ablative component, respectively.
403 The parameters ξ_0 , ξ_1 , and ξ_2 control the heat flux magnitude, spatial variation, and temporal
404 variation, respectively. The constant α_i is a small material-dependent constant determined
405 from the B' table [9], specifying the surface recession velocity for a given change in surface
406 temperature.

407 4.3 Data Generation

408 Full-order solutions of the TPS are computed using the FEM multi-mechanics module of
409 the **Aria** package [4], where the mesh is shown in Fig. 2. The mesh consists of 2196 to-
410 tal elements, with 366 elements for each ablative component and 1098 elements for the
411 substrate component. All solutions are computed for one minute from an uniform ini-
412 tial temperature of $T(x, t_0) = 300$ K. Given an operating condition $\boldsymbol{\xi} = [\boldsymbol{\xi}_{\text{BC}}, \boldsymbol{\xi}_{\text{SRM}}]^\top$, a
413 full-order solution consists of then collection of time-varying temperature and displacement
414 fields $\left\{ \left(t_k, \mathbf{u}_{\text{HF}}^{(l)}(t_k), \mathbf{w}_{\text{HF}}^{(l)}(t_k), \boldsymbol{\xi}^{(l)} \right) \right\}_{k=0}^{p-1}$, where p is the number of time steps with a step size
415 of $\Delta t \approx 10^{-3}$. The observable trajectories are representative of near-wall thermocouple
416 sensing of hypersonic flows involving heat transfer. At each time instance t_k , a tempera-
417 ture reading is recorded from each ablative component using the thermocouples shown in
418 Fig. 2, resulting in three temperature signals, i.e., the observables $\mathbf{z}_{textHF} \in \mathbb{R}^3$. Therefore,
419 each full-order solution produces one trajectory of observables $\left\{ \left(t_k, \mathbf{z}_{\text{HF}}^{(l)}(t_k), \boldsymbol{\xi}^{(l)} \right) \right\}_{k=0}^{p-1}$. The
420 goal of the PIROM is to predict the surface temperature and displacement as accurately as
421 possible.

422 4.3.1 Definition of Training and Testing Datasets

423 The range of parameters used to generate the training \mathcal{D}_1 and testing $\{\mathcal{D}_2, \mathcal{D}_3\}$ datasets
424 are listed in Table 1. The training and testing datasets are designed, respectively, to: (1)
425 minimize the information that the PIROM can “see”, and (2) to maximize the variabil-
426 ity of test operating conditions to examine the PIROM's generalization performance. A
427 total of 110 normally-distributed data points for the BC parametrization are visualized in
428 Fig. 3(a), and the corresponding observable trajectories are shown in Figs. 3(b) and 3(c).
429 The training dataset \mathcal{D}_1 includes 10 trajectories with randomly selected BC parameters from
430 the 110 points, with nominal SRM parameters $\boldsymbol{\xi}_{\text{SRM}} = \{1, 1, 1\} \times 10^{-6}$. Note that although
431 Fig. 3(c) shows the surface displacements for all ablative components in \mathcal{D}_1 , only the *surface*
432 *temperature is used for training the PIROM.*

433 Two additional datasets are generated for testing. The dataset \mathcal{D}_2 includes the remaining
434 100 BC parameter values not considered in \mathcal{D}_1 , and the high-fidelity simulation are generated
435 with the same nominal SRM parameters. The cases in the \mathcal{D}_3 fixes the boundary condition
436 as shown in Fig. 3(a) and varies the SRM parameters as shown in Table. 1. The testing
437 datasets \mathcal{D}_2 and \mathcal{D}_3 are *out-of-distribution* (OOD) datasets, and are meant for testing the

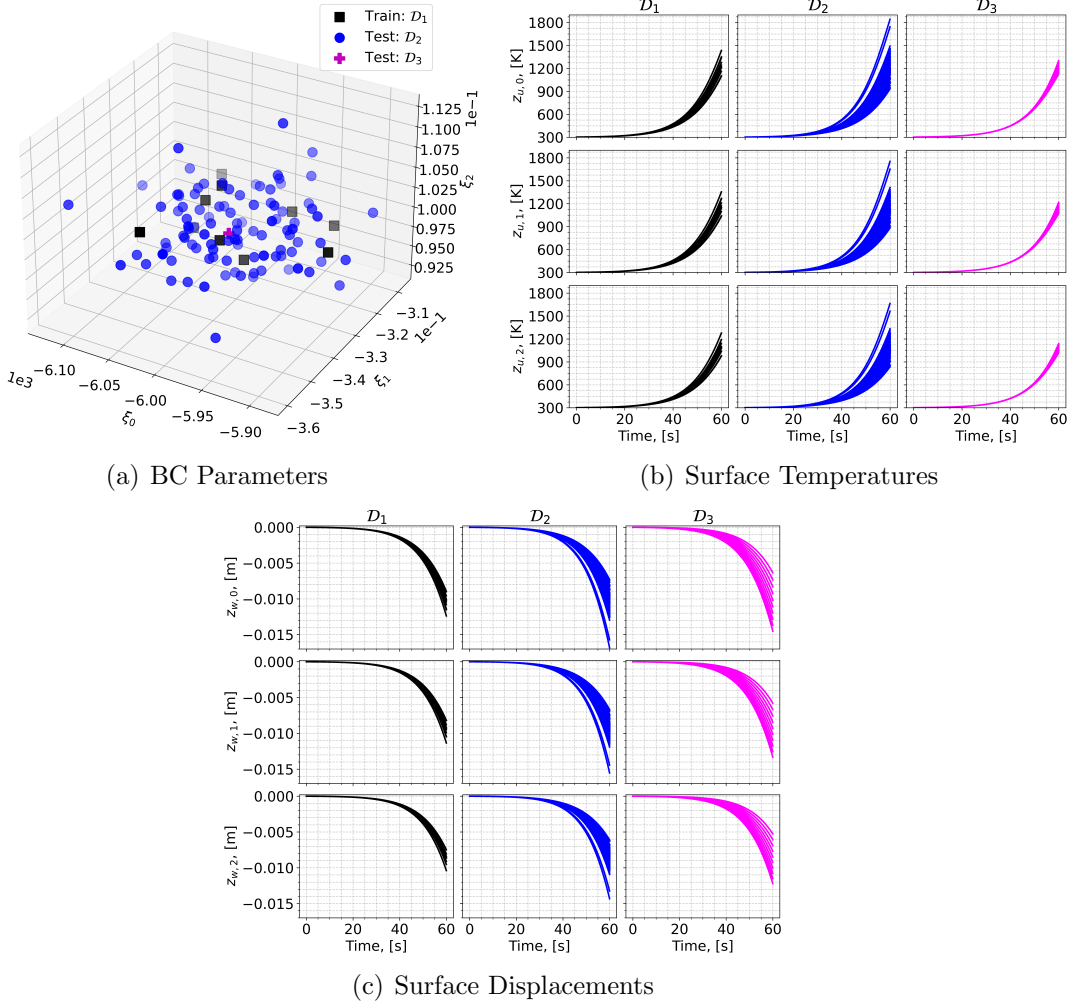


Figure 3: Boundary condition parameters, temperature observables, and displacement observables for the training and testing datasets. The variables $z_{u,i}$ and $z_{w,i}$ correspond to the surface temperature and displacement of the i -th ablative component, respectively.

438 generalizability of the ROMs to unseen BCs and SRMs, respectively.

439 4.4 Performance Metrics

440 The performance of the PIROM is evaluated by the metrics of prediction error and compu-
441 tational cost.

442 **Prediction Error** Consider one trajectory of high-fidelity surface temperature and dis-
443 placement data $\left\{ \left(t_k, \mathbf{z}_{u,\text{HF}}^{(l)}(t_k), \mathbf{z}_{w,\text{HF}}^{(l)}(t_k) \right) \right\}_{k=0}^{p-1}$ for the l -th operating condition in the testing
444 datasets \mathcal{D}_2 or \mathcal{D}_3 . The difference $e_i^{(l)}$ for the i -th predicted observable, denoted as $\hat{z}_i^{(l)}$, is

445 computed as,

$$e_i^{(l)} = \frac{1}{\Delta z_i^{(l)}} \sqrt{\frac{1}{p} \sum_{k=0}^{p-1} \left(z_{i,\text{HF}}^{(l)}(t_k) - z_i^{(l)}(t_k) \right)^2} \quad (48)$$

446 for $i = 1, 2, 3$ and $z_i^{(l)} \in \{z_{i,u}^{(l)}, z_{i,w}^{(l)}\}$, and where,

$$\Delta z_i^{(l)} = \max_{0 \leq k \leq p-1} z_{i,\text{HF}}^{(l)}(t_k) - \min_{0 \leq k \leq p-1} z_{i,\text{HF}}^{(l)}(t_k) \quad (49)$$

447 Subsequently, the prediction error of one trajectory is computed by a weighted sum based
 448 on the area of each *ablative component*, resulting in the normalized root mean square error
 449 (NRMSE) metric for one trajectory,

$$\text{NRMSE} = \frac{\sum_{i=1}^{\tilde{N}} |\Omega_i| e_i^{(l)}}{\sum_{i=1}^{\tilde{N}} |\Omega_i|} \times 100\% \quad (50)$$

450 For one dataset, the NRMSE is defined to be the average of the NRMSEs of all trajectories
 451 in the dataset.

452 **Computational Acceleration** The *computational acceleration* metric focuses on the quan-
 453 tification of the speedup factor $\frac{\mathcal{T}_{\text{HF}}(\mathcal{D})}{\mathcal{T}_{\mathcal{M}}(\mathcal{D})}$, where $\mathcal{T}_{\text{HF}}(\mathcal{D})$ and $\mathcal{T}_{\mathcal{M}}(\mathcal{D})$ correspond to the wall-clock
 454 time required by the high-fidelity model and the reduced-order model \mathcal{M} (i.e., PIROM or
 455 RPM) to evaluate all trajectories in the dataset \mathcal{D} , respectively. For a benchmark analysis
 456 of the computational costs during the training phase, please refer to Ref. [13].

457 4.5 Generalization to Boundary Conditions

458 To assess generalization to BC, the PIROM and RPM are evaluated on the \mathcal{D}_2 dataset. Tem-
 459 perature trajectory predictions for a representative test case are shown in Figs. 4(a) and 4(b),
 460 where the PIROM accurately captures the surface temperature and displacement dynamics,
 461 while the RPM exhibits larger deviations and under-predicts surface displacements due to
 462 the averaging effects of the LCM. The mean NRMSE across all test cases in \mathcal{D}_2 is shown
 463 in Figs. 4(e) and 4(f), where the PIROM consistently achieves errors of $\approx 0.5\%$ for both
 464 temperature and displacement predictions, improving the RPM's accuracy by an order of
 465 magnitude. Figure 4 reports the average substrate temperature, where the LCM remains
 466 highly accurate due to the symmetric TPS geometry, adiabatic BCs, and negligible thermal
 467 gradients within the substrate. Although the PIROM is trained only on the surface tem-
 468 peratures of the three ablative components, its hidden dynamics retain the LCM's accuracy
 469 for this untrained observable, demonstrating the PIROM's ability to generalize and preserve
 470 the underlying physics of the reduced-physics backbone.

471 **4.6 Generalization to Surface Recession Models**

472 The generalization performance of the PIROM and RPM is also evaluated on surface recess-
473 sion models using the \mathcal{D}_3 dataset. As detailed in Table 1, the SRM parameter α in \mathcal{D}_3 is
474 perturbed 10 times by up to $\pm 50\%$ from their nominal values. The SRM model perturbation
475 introduces significant changes to the ablative layer dynamics, potentially increasing the rate
476 of ablation at lower temperatures, as shown in Figs. 4(c) and 4(d). The PIROM, without
477 considering any SRM variations during training, is able to accurately predict the surface tem-
478 perature and displacement dynamics for the perturbed SRMs. Figures 4(e) and 4(f) show
479 the mean NRMSE across all test cases in \mathcal{D}_3 , where the PIROM consistently achieves errors
480 below 1.5% for both temperature and displacement predictions, and consistently improves
481 the RPM’s accuracy by approximately an order of magnitude.

482 **4.7 Computational Cost**

483 All computations are performed in serial for fairness on an Intel Xeon (R) Gold 6258R
484 CPU 2.70GHz computer with 62 GB of RAM. The numerical integration for the RPM
485 and PIROM models are performed using SciPy’s `solve_ivp` function with default settings.
486 Provided a parametrization for the BC and SRM, the high-fidelity FEM simulation takes
487 about ≈ 60 seconds, the RPM takes about ≈ 0.137 seconds, and the PIROM takes about
488 ≈ 0.280 seconds. Therefore, during evaluation both the RPM and PIROM achieve speedup
489 factors of approximately 438 and 214, respectively, over the high-fidelity model. As a result,
490 the PIROM and RPM are *two-orders-of-magnitude faster* than the high-fidelity model. The
491 PIROM nearly preserves the computational efficiency of the RPM (about twice as expensive
492 as the RPM), while achieving significantly higher accuracy and generalization capabilities.
493 The results demonstrate the benefits of physics-infused modeling for the development of
494 efficient and generalizable ROMs for complex multi-physics systems.

495 **4.8 Summary of Results**

496 The results presented in this section demonstrate the accuracy, generalizability, and com-
497 putational efficiency of the proposed PIROM approach for the analysis of thermo-ablative
498 multi-layered hypersonic TPS. The PIROM consistently achieves low prediction errors below
499 1% for both surface temperature and displacement across a range of unseen boundary con-
500 ditions and surface recession models. Furthermore, the PIROM retains the computational
501 efficiency of traditional RPMs, achieving speedup factors of over 200 times compared to high-
502 fidelity FEM simulations. The generalization capabilities of the PIROM are attributed to its
503 hybrid structure: a physics-based LCM backbone that ensures consistency with the under-
504 lying thermodynamics, while a data-driven correction mechanism captures the un-resolved
505 dynamics.

506 **5 Conclusions**

507 This work presents the development and validation of the *scientific machine learning* frame-
508 work termed *Physics-Informed Reduced Order Model* (PIROM) for simulating the transient

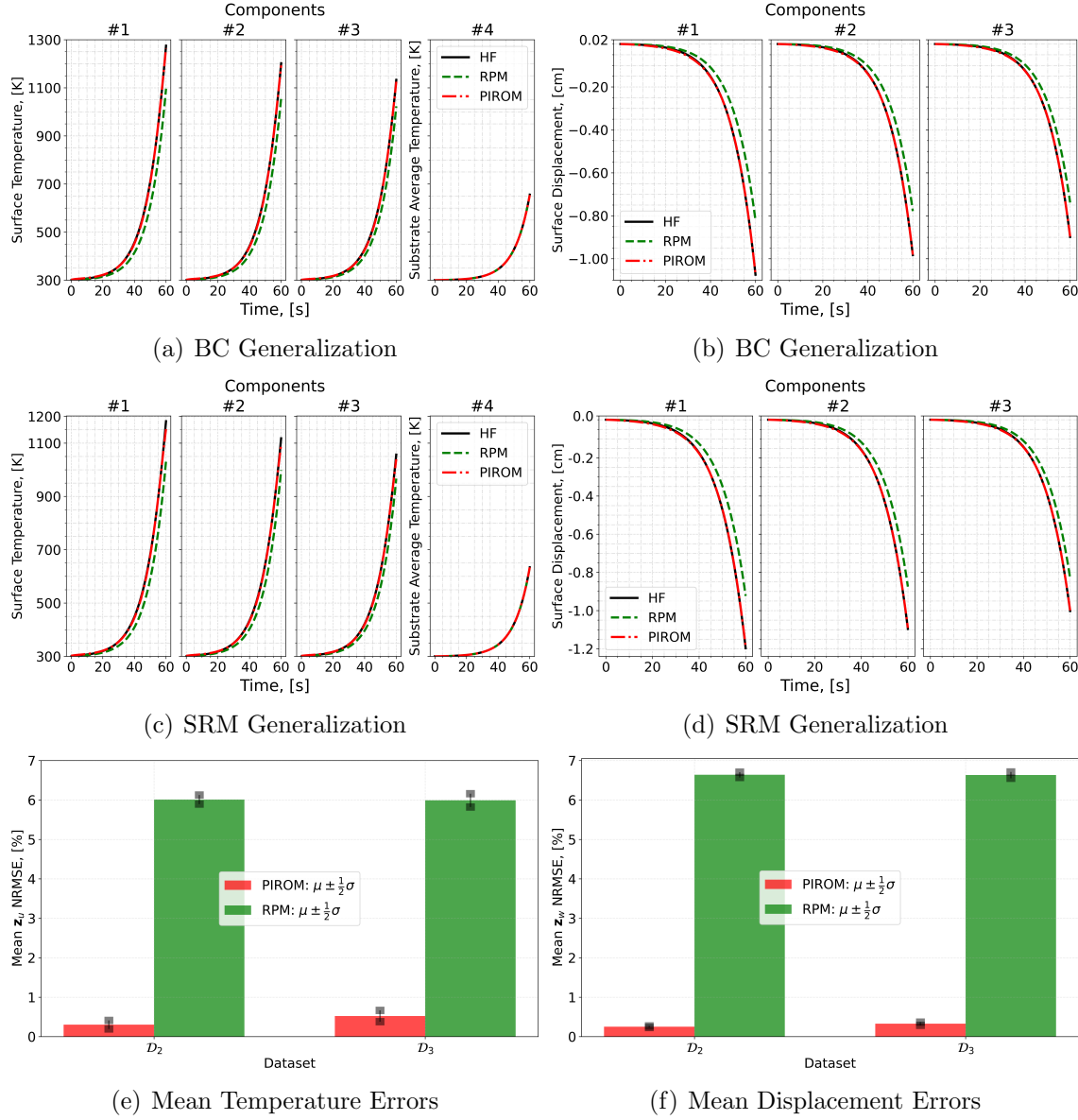


Figure 4: PIROM predictions against high-fidelity solutions for (a)-(b) BC generalization, (c)-(d) SRM generalization, and (e)-(f) mean errors across testing datasets.

509 thermo-ablative response of hypersonic thermal protection systems (TPS) subjected to hy-
510 personic aerodynamic heating. Using coarse-graining on a DG-FEM model and the Mori-
511 Zwanzig formalism, the PIROM formulation in Ref. [13] is extended to account for non-
512 decomposing ablative material response. The PIROM builds upon the following two key
513 components: (1) a first-order physics-based model, i.e., the LCM and SRM, for low-fidelity
514 predictions of the transient thermo-ablative TPS response; and (2) a data-driven closure to
515 the non-Markovian term in the generalized Langevin equation (GLE). The non-Markovian
516 closure is recast as a set of hidden states that evolve according to a data-driven dynamical
517 system that is learned from a sparse collection of high-fidelity temperature signals.

518 The results demonstrate that the PIROM framework effectively reconciles the trade-
519 offs between accuracy, generalizability, and efficiency of the ITM for simulating ablating
520 hypersonic TPS. The PIROM consistently achieves mean observable prediction errors of
521 $\approx 0.5\%$ for a wide range of extrapolative settings of model parameters, involving time-and-
522 space varying boundary conditions and SRM models. Notably, the PIROM improves the
523 RPM's accuracy by an order of magnitude while preserving its computational efficiency,
524 physical interpretability, and parametric generalizability. Moreover, the PIROM delivers
525 online evaluations that are two orders of magnitude faster than the FOM. These results
526 highlight the PIROM's potential as a promising framework for optimizing multi-physical
527 dynamical systems, such as TPS under diverse operating conditions.

528 A Technical Details

529 This appendix presents the technical details of the PIROM framework applied to the TPS
 530 ablation problem. The first section provides the mathematical details for the definition of
 531 the DG-FEM. The second section follows the projection procedures from Ref. [\[x\]](#), and demon-
 532 strates the effects of coarse-graining on the advection matrix. The third section presents the
 533 derivation of the LCM model from an energy-conservation perspective.

534 A.1 Full-Order Model

535 To obtain the full-order numerical solution, the governing equation is spatially discretized
 536 using variational principles of Discontinuous Galerkin (DG) to result in a high-dimensional
 537 system of ordinary differential equations (ODEs). The DG-FEM model is written in an
 538 element-wise form, which is beneficial for subsequent derivations of the lower-order models.
 539 Note that the choice of DG approach here is mainly for theoretical convenience in the sub-
 540 sequent coarse-graining formulation. In the numerical results, the full-order TPS ablation
 541 simulations is computed using standard FEM instead, and the equivalence between DG and
 542 standard FEM is noted upon their convergence.

543 A.1.1 Domain Discretization

544 Consider a conforming mesh partition of the domain, as shown in Fig. [DOMAIN](#), where each
 545 element belongs to one and only one component. Denote the collection of all M elements
 546 as $\{E_i\}_{i=1}^M$. To ease the description of the DG model, a graph structure is employed. The
 547 elements are treated as vertices, the set of which is denoted $\mathcal{V} = \{m\}_{m=1}^M$. Two neighboring
 548 elements, E_i and E_j , are connected by an edge (i, j) , and the shared boundary between them
 549 is denoted e_{ij} . The collection of all edges are denoted \mathcal{E} , and \mathcal{G} is referred to as a graph.
 550 In the graph, the edges are unidirected, meaning if $(i, j) \in \mathcal{E}$ then $(j, i) \in \mathcal{E}$. Furthermore,
 551 denote the neighbors of the i -th element as $\mathcal{N}_i = \{j | (i, j) \in \mathcal{E}\}$. Lastly, for the ease of
 552 notation, introduce two special indices: T for the boundary of an element that overlaps with
 553 the Dirichlet boundary condition, and similarly q for the Neumann boundary condition.

554 A.1.2 Weak Form of Discontinuous Galerkin Method

555 Choosing appropriate basis functions ϕ_k and ϕ_l and using the Interior Penalty Galerkin
 556 (IPG) scheme [5], the variational bilinear form for eq. (1a) is,

$$\sum_{i=1}^M a_{\epsilon,i}(\phi_k, \phi_l) = \sum_{i=1}^M L_i(\phi_k) \quad (51)$$

557 where ϵ is an user-specified parameter and,

$$a_{\epsilon,i}(\phi_k, \phi_l) = \int_{E^{(i)}} \left(\rho c_p \phi_k \frac{\partial \phi_l}{\partial t} + \nabla \phi_k \cdot (\mathbf{k} \nabla \phi_l) - \rho c_p \phi_k \mathbf{v} \cdot \nabla \phi_l \right) dE^{(i)} \quad (52a)$$

$$\begin{aligned} &= - \sum_{j \in \mathcal{N}_i \cup \{T_b\}} \int_{e_{ij}} \{ \mathbf{k} \nabla \phi_k \cdot n \} [\phi_l] de_{ij} + \epsilon \sum_{j \in \mathcal{N}_i \cup \{T_b\}} \int_{e_{ij}} \{ \mathbf{k} \nabla \phi_l \cdot n \} [\phi_k] de_{ij} \\ &\quad + \sigma \sum_{j \in \mathcal{N}_i \cup \{T_b\}} \int_{e_{ij}} [\phi_k] [\phi_l] de_{ij} \end{aligned} \quad (52b)$$

$$L_i(v) = \epsilon \sum_{j \in \mathcal{N}_i \cup \{T_b\}} \int_{e_{ij}} (\mathbf{k} \nabla \phi_l \cdot n) T_b de_{ij} + \int_{e_{iq}} \phi_k q_b de_{iq} + \sigma \int_{e_{iT}} \phi_k T_b de_{iT} \quad (52c)$$

558 In the bi-linear form above, the notations $[]$ and $\{ \}$ are respectively the jumps and averages
559 at the boundary e_{ij} share by two elements E_i and E_j ,

$$[u] = u|_{E_i} - u|_{E_j}, \quad \{u\} = \frac{1}{2} \left(u|_{E_i} + u|_{E_j} \right), \quad \text{for } x \in e_{ij} = E_i \cap E_j$$

560 Furthermore, in the bi-linear form, the terms associated with σ are introduced to enforce
561 the Dirichlet boundary conditions; σ is a penalty factor whose value can depend on the size
562 of an element. Depending on the choice of ϵ , the bi-linear form corresponds to symmetric
563 IPG ($\epsilon = -1$), non-symmetric IPG ($\epsilon = 1$), and incomplete IPG ($\epsilon = 0$). All these schemes
564 are consistent with the original PDE and have similar convergence rate with respect to mesh
565 size. In the following derivations, the case $\epsilon = 0$ is chosen for the sake of simplicity.

566 A.1.3 Discontinuous Galerkin Model

567 Next, the DG-based model is written in an element-wise form. For the i -th element, use a
568 set of P trial functions to represent the temperature as in eq. (6). Without loss of generality,
569 the trial functions are assumed to be orthogonal, so that $\int_{E^{(i)}} \phi_k^{(i)}(x) \phi_l^{(i)}(x) dx = |E^{(i)}| \delta_{kl}$,
570 where $|E^{(i)}|$ is the area ($n_d = 2$) or volume ($n_d = 3$) of the i -th element, and δ_{kl} is the
571 Kronecker delta.

572 Using test functions same as trial functions, the dynamics $\mathbf{u}^{(i)}$ is obtained by evaluating
573 the element-wise bi-linear forms,

$$a_{\epsilon,i}(\phi_k^{(i)}, T^{(i)}) = L_i(\phi_k^{(i)}), \quad k = 1, 2, \dots, P \quad (53)$$

574 The above procedure yields,

$$\mathbf{A}^{(i)} \dot{\mathbf{u}}^{(i)} = (\mathbf{B}^{(i)} + \mathbf{C}^{(i)}(t)) \mathbf{u}^{(i)} + \sum_{j \in \mathcal{N}_i \cup \{T_b\}} \left(\mathbf{B}_{ij}^{(i)} \mathbf{u}^{(i)} + \mathbf{B}_{ij}^{(j)} \mathbf{u}^{(j)} \right) + \mathbf{f}^{(i)}(t) \quad (54)$$

575 where for $k, l = 1, 2, \dots, P$,

$$[\mathbf{A}^{(i)}]_{kl} = \int_{E^{(i)}} \rho c_p \phi_k^{(i)} \phi_l^{(i)} dE^{(i)} \quad (55a)$$

$$[\mathbf{B}^{(i)}]_{kl} = - \int_{E^{(i)}} (\nabla \phi_k^{(i)}) \cdot (\mathbf{k} \nabla \phi_l^{(i)}) dE^{(i)} \quad (55b)$$

$$[\mathbf{C}^{(i)}]_{kl} = \int_{E^{(i)}} \rho c_p \phi_k^{(i)} \mathbf{v}^{(i)} \cdot \nabla \phi_l^{(i)} dE^{(i)} \quad (55c)$$

$$[\mathbf{B}_{ij}^{(i)}] = \int_{e_{ij}} \left\{ \mathbf{k} \nabla \phi_k^{(i)} \cdot \hat{n} \right\} \phi_l^{(i)} - \sigma [\phi_k^{(i)}] \phi_l^{(i)} de_{ij} \quad (55d)$$

$$[\mathbf{B}_{ij}^{(j)}] = \int_{e_{ij}} - \left\{ \mathbf{k} \nabla \phi_k^{(i)} \cdot \hat{n} \right\} \phi_l^{(j)} + \sigma [\phi_k^{(i)}] \phi_l^{(j)} de_{ij} \quad (55e)$$

$$[\mathbf{f}^{(i)}]_k = \int_{e_{iq}} \phi_k^{(i)} q_b de_{iq} + \sigma \int_{e_{iT}} \phi_k^{(i)} de_{iT} \quad (55f)$$

576 The matrices $\mathbf{A}^{(i)} \in \mathbb{R}^{P \times P}$, $\mathbf{B}^{(i)} \in \mathbb{R}^{P \times P}$, and $\mathbf{C}^{(i)} \in \mathbb{R}^{P \times P}$ are respectively the capacitance,
 577 conductivity, and advection matrices for element i . These matrices depend on ρ , c_p , \mathbf{k} , and
 578 \mathbf{v} , and hence can be non-linear functions of $\mathbf{u}^{(i)}$. Since the trial functions are orthogonal, if
 579 ρc_p is constant within an element, $\mathbf{A}^{(i)}$ is diagonal; otherwise, \mathbf{A}_i is symmetric and positive
 580 definite as $\rho c_p > 0$.

581 For compactness, the element-wise model in eq. (54) is also written in matrix form,

$$\mathbf{A}(\dot{\mathbf{u}}) = [\mathbf{B}(\mathbf{u}) + \mathbf{C}(\mathbf{u})] \mathbf{u} + \mathbf{f}(t) \quad (56)$$

582 where $\mathbf{u} = [\mathbf{u}^{(1)}, \mathbf{u}^{(2)}, \dots, \mathbf{u}^{(M)}]^T \in \mathbb{R}^{MP}$ includes all DG variables, $\mathbf{f} = [\mathbf{f}^{(1)}, \mathbf{f}^{(2)}, \dots, \mathbf{f}^{(M)}]^T \in$
 583 \mathbb{R}^{MP} , \mathbf{A} and \mathbf{C} are matrices of M diagonal blocks whose i -th blocks are $\mathbf{A}^{(i)}$ and $\mathbf{C}^{(i)}$, and
 584 \mathbf{B} is a matrix of $M \times M$ blocks whose (i, j) -th block is,

$$\mathbf{B}_{ij} = \begin{cases} \mathbf{B}^{(i)} + \sum_{j \in \mathcal{N}_i \cup \{T_b\}} \mathbf{B}_{ij}^{(i)}, & i = j \\ \mathbf{B}_{ij}^{(j)}, & i \neq j \end{cases} \quad (57)$$

585 The dependency of \mathbf{A} , \mathbf{B} , and \mathbf{C} on \mathbf{u} is explicitly noted in eq. (56), which is the source of
 586 non-linearity in the current TPS problem. Moreover, the mesh velocity \mathbf{v} varies with space
 587 and time, and thus the advection matrix \mathbf{C} varies with time as a function of q_b .

588 A.2 Coarse-Graining of Dynamics

589 The LCM is obtained by coarse-graining the full-order DG-FEM. This coarse-graining proce-
 590 dure produces resolved $\mathbf{r}^{(1)}(\mathbf{u}, t)$ and residual $\mathbf{r}^{(2)}(\mathbf{u}, t)$ dynamics as in eq. (23). This section
 591 presents the detail derivations and magnitude analysis for the resolved and residual dynam-
 592 ics.

593 **A.2.1 Resolved Dynamics**

594 Using eq. (20), the resolved dynamics is computed as follows,

$$\mathbf{r}^{(1)}(\mathbf{u}, t) = \mathcal{P} [\Phi^+ \mathbf{A}(\mathbf{u})^{-1} (\mathbf{B}(\mathbf{u})\mathbf{u} + \mathbf{C}(\mathbf{u})\mathbf{u} + \mathbf{f}(t))] \quad (58a)$$

$$= \Phi^+ \mathbf{A}(\mathbf{P}\mathbf{u})^{-1} \mathbf{P}\mathbf{B}(\mathbf{P}\mathbf{u}) \mathbf{P}\mathbf{u} + \Phi^+ \mathbf{A}(\mathbf{P}\mathbf{u})^{-1} \mathbf{P}\mathbf{C}(\mathbf{P}\mathbf{u}) \mathbf{P}\mathbf{u} \\ + \Phi^+ \mathbf{A}(\mathbf{P}\mathbf{u})^{-1} \mathbf{P}\mathbf{f}(t, \mathbf{P}\mathbf{u}) \quad (58b)$$

$$= \underbrace{\Phi^+ \mathbf{A}(\Phi\bar{\mathbf{u}})^{-1} \Phi}_{\#1} \underbrace{\Phi^+ \mathbf{B}(\Phi\bar{\mathbf{u}}) \Phi\bar{\mathbf{u}}}_{\#2} + \Phi^+ \mathbf{A}(\Phi\bar{\mathbf{u}})^{-1} \Phi \underbrace{\Phi^+ \mathbf{C}(\Phi\bar{\mathbf{u}}) \Phi\bar{\mathbf{u}}}_{\#3} \\ + \Phi^+ \mathbf{A}(\Phi\bar{\mathbf{u}})^{-1} \Phi \underbrace{\Phi^+ \mathbf{f}(t, \Phi\bar{\mathbf{u}})}_{\#4} \quad (58c)$$

595 Detailed derivations for the #1, #2, and #4 terms can be found in Ref. [x]. The effects of
596 coarse-graining on the advection term #3 are analyzed next.

597 **Term #3** The $\mathbf{C}(\mathbf{u}) \in \mathbb{R}^{MP \times MP}$ matrix contains M diagonal of size $P \times P$, since the
598 basis functions are defined locally on each element. Therefore, $[\mathbf{C}(\mathbf{u})]_{ij} = \mathbf{0}$ for all $i \neq j$ with
599 $i, j = 1, 2, \dots, M$. It follows that for $k, l = 1, 2, \dots, N$,

$$[\Phi^+ \mathbf{C}(t, \Phi\bar{\mathbf{u}}) \Phi]_{kl} = \sum_{i=1}^M \sum_{j=1}^M \boldsymbol{\varphi}_i^{k+} [\mathbf{C}(t, \Phi\bar{\mathbf{u}})]_{ij} \boldsymbol{\varphi}_j^l \quad (59a)$$

$$= \sum_{i=1}^M \boldsymbol{\varphi}_i^{k+} [\mathbf{C}(t, \Phi\bar{\mathbf{u}})]_{ii} \boldsymbol{\varphi}_i^l \quad (59b)$$

$$= \sum_{i \in \mathcal{V}_k} \boldsymbol{\varphi}_i^{k+} [\mathbf{C}(t, \Phi\bar{\mathbf{u}})]_{ii} \boldsymbol{\varphi}_i^l \quad (59c)$$

600 where in the second row, the fact that $[\mathbf{C}(\mathbf{u})]_{ij} = 0$ for all $i \neq j$ is used, and in the last row,
601 the fact that $\boldsymbol{\varphi}_i^{k+} = 0$ for all $i \notin \mathcal{V}_k$ is used. Now, considering that $[\mathbf{C}(\mathbf{u})]_{ii}$ has a (1, 1)-th
602 zero element, i.e., $[\mathbf{C}(t, \Phi\bar{\mathbf{u}})]_{ii} = 0$, and that if $k \neq l$ then $i \notin \mathcal{V}_l$ and thus $\boldsymbol{\varphi}_i^l = \mathbf{0}$, it follows
603 that for some index $i \in \mathcal{V}_k$,

$$\boldsymbol{\varphi}_i^{k+} [\mathbf{C}(t, \Phi\bar{\mathbf{u}})]_{ii} \boldsymbol{\varphi}_i^l = \boldsymbol{\varphi}_i^{k+} [\mathbf{C}(t, \Phi\bar{\mathbf{u}})]_{ii} \boldsymbol{\varphi}_i^k = \frac{|E_i|}{|\Omega_k|} [C_{11}(t, \Phi\bar{\mathbf{u}})]_{ii} = 0 \quad (60)$$

604 The matrix $[\Phi^+ \mathbf{C}(t, \Phi\bar{\mathbf{u}}) \Phi]_{kl} = 0$ for all $k, l = 1, 2, \dots, N$, and thus,

$$\bar{\mathbf{C}}(t, \bar{\mathbf{u}}) = \Phi^+ \mathbf{C}(t, \Phi\bar{\mathbf{u}}) \Phi = \mathbf{0} \quad (61)$$

605 as indicated by the LCM in eq. (9).

606 **A.2.2 Magnitude Analysis for Residual Dynamics**

607 Next, the magnitude of the residual dynamics $\mathbf{r}^{(2)}(\mathbf{u}, t)$ is analyzed to pinpoint the missing
608 physics in the LCM. By definition,

$$\mathbf{r}^{(2)}(\mathbf{u}, t) = \dot{\bar{\mathbf{u}}} - \mathbf{r}^{(1)}(\bar{\mathbf{u}}, t) \quad (62a)$$

$$= \Phi^+ \mathbf{r}(\mathbf{u}, t) - \mathbf{r}^{(1)}(\mathbf{u}, t) \quad (62b)$$

$$\begin{aligned} &= \underbrace{\Phi^+ \mathbf{A}(\mathbf{u})^{-1} \mathbf{B}(\mathbf{u}) \mathbf{u} - \bar{\mathbf{A}}(\bar{\mathbf{u}})^{-1} \bar{\mathbf{B}}(\bar{\mathbf{u}}) \bar{\mathbf{u}}}_{\#1} + \underbrace{\Phi^+ \mathbf{A}(\mathbf{u})^{-1} \mathbf{C}(\mathbf{u}) \mathbf{u} - \bar{\mathbf{A}}(\bar{\mathbf{u}})^{-1} \bar{\mathbf{C}}(t, \bar{\mathbf{u}}) \bar{\mathbf{u}}}_{\#2} \\ &\quad + \underbrace{\Phi^+ \mathbf{A}(\mathbf{u})^{-1} \mathbf{f}(t) - \bar{\mathbf{A}}(\bar{\mathbf{u}})^{-1} \bar{\mathbf{f}}(t)}_{\#3} \end{aligned} \quad (62c)$$

609 The magnitude analysis for terms $\#1$ and $\#3$ can be found in Ref. [x]. The analysis for term
610 $\#2$ is presented next. Let $\mathbf{D}(\bar{\mathbf{u}}) = \mathbf{A}(\Phi \bar{\mathbf{u}})^{-1} \mathbf{P} \mathbf{C}(t, \Phi \bar{\mathbf{u}})$, then,

$$\Phi^+ \mathbf{A}(\mathbf{u})^{-1} \mathbf{C}(\mathbf{u}) \mathbf{u} - \bar{\mathbf{A}}(\bar{\mathbf{u}})^{-1} \bar{\mathbf{C}}(t, \bar{\mathbf{u}}) \bar{\mathbf{u}} \quad (63a)$$

$$= \Phi^+ \mathbf{A}(\mathbf{u})^{-1} \mathbf{C}(\mathbf{u}) \mathbf{u} - \Phi^+ \mathbf{A}(\Phi \bar{\mathbf{u}})^{-1} \mathbf{P} \mathbf{C}(t, \Phi \bar{\mathbf{u}}) \Phi \Phi^+ \mathbf{u} \quad (63b)$$

$$= \Phi^+ \mathbf{A}^{-1}(\mathbf{u}) \mathbf{C}(\mathbf{u}) \mathbf{u} - \Phi^+ \mathbf{D}(\bar{\mathbf{u}}) \Phi \Phi^+ \mathbf{u} \quad (63c)$$

$$(63d)$$

611 where $\mathbf{P} = \Phi \Phi^+$. Thus,

$$\|\Phi^+ \mathbf{A}(\mathbf{u})^{-1} \mathbf{C}(\mathbf{u}) \mathbf{u} - \bar{\mathbf{A}}(\bar{\mathbf{u}})^{-1} \bar{\mathbf{C}}(t, \bar{\mathbf{u}}) \bar{\mathbf{u}}\| \quad (64a)$$

$$\leq \|\Phi^+ \mathbf{A}^{-1}(\mathbf{u}) \mathbf{C}(\mathbf{u}) \mathbf{u} - \Phi^+ \mathbf{D}(\bar{\mathbf{u}}) \mathbf{u}\| + \|\Phi^+ \mathbf{D}(\bar{\mathbf{u}}) \mathbf{u} - \Phi^+ \mathbf{D}(\bar{\mathbf{u}}) \Phi \Phi^+ \mathbf{u}\| \quad (64b)$$

$$\leq \|\Phi^+\| \underbrace{\|\mathbf{A}^{-1}(\mathbf{u}) \mathbf{C}(\mathbf{u}) \mathbf{u} - \mathbf{D}(\bar{\mathbf{u}}) \mathbf{u}\|}_{\#1} + \|\Phi^+ \mathbf{D}(\bar{\mathbf{u}})\| \underbrace{\|\mathbf{u} - \Phi \Phi^+ \mathbf{u}\|}_{\#2} \quad (64c)$$

612 where term $\#2$ is due to the approximation of non-uniform temperature as constants, and
613 term $\#1$ is the error in the advection dynamics due to coarse-graining.

614 **A.3 Lumped Capacitance Model**

615 The following assumptions are employed: (1) the temperature in component (i) is described
616 by a scalar time-varying average temperature $\bar{u}^{(i)}$, (2) between neighboring components (i)
617 and (j) the heat flux is approximated as,

$$q_{ij} = \frac{\bar{u}^{(j)} - \bar{u}^{(i)}}{R_{ij}} \quad (65)$$

618 where R_{ij} is the thermal resistance. Empirically, for a component of isotropic heat conduction
619 with thermal conductivity k , length ℓ , and cross-section area A , the thermal resistance is $R = \ell/kA$. Between
620 components i and j , define $R_{ij} = R_i + R_j$. In addition, the heat flux due to Dirichlet
621 boundary condition is computed as $q_{iT} = (T_b - \bar{u}^{(i)})/R_i$.

622 At component i , the dynamics of LCM are given by,

$$\int_{E^{(i)}} \rho c_p \dot{\bar{u}}^{(i)} dE^{(i)} = \left(\sum_{j \in \mathcal{N}_i} \int_{e_{ij}} \frac{\bar{u}^{(j)} - \bar{u}^{(i)}}{R_{ij}} de_{ij} \right) + \int_{e_{iq}} q_b de_{iq} + \int_{e_{iT}} \frac{T_b - \bar{u}^{(i)}}{R_i} de_{iT} \quad (66a)$$

$$\bar{A}^{(i)} \dot{\bar{u}}^{(i)} = \left(\sum_{j \in \mathcal{N}_i} \frac{|e_{ij}|}{R_{ij}} (\bar{u}^{(j)} - \bar{u}^{(i)}) \right) + |e_{iq}| \bar{q}^{(i)} + \frac{|e_{iT}|}{R_i} (\bar{T}^{(i)} - \bar{u}^{(i)}) \quad (66b)$$

$$= \sum_{j \in \mathcal{N}_i} \left(-\frac{|e_{ij}|}{R_{ij}} \bar{u}^{(i)} + \frac{|e_{ij}|}{R_{ij}} \bar{u}^{(j)} \right) + \left(-\frac{|e_{iT}|}{R_i} \bar{u}^{(i)} \right) + \left(|e_{iq}| \bar{q}^{(i)} + \frac{|e_{iT}|}{R_i} \bar{T}^{(i)} \right) \quad (66c)$$

$$= \sum_{j \in \mathcal{N}_i \cup \{T_b\}} \left(\bar{B}_{ij}^{(i)} \bar{u}^{(i)} + \bar{B}_{ij}^{(j)} \bar{u}^{(j)} \right) + \bar{f}^{(i)} \quad (66d)$$

623 where in eq. (66b) $|e|$ denotes the length ($d = 2$) or area ($d = 3$) of a component boundary
624 e . The $\bar{A}^{(i)}$, $\bar{B}_{ij}^{(i)}$, and $\bar{B}_{ij}^{(j)}$ quantities are provided in eq. (12).

625 The lumped-mass representation for the four-component TPS is shown in Fig. ???. Let
626 v_i represent the area of the i -th element, $\overline{\rho c_p}_i$, the heat capacity evaluated using the average
627 temperature $\bar{u}^{(i)}$, and $1/R_{ij} = 1/R_i(\bar{u}^{(i)}) + 1/R_j(\bar{u}^{(j)})$ the equivalent thermal resistance
628 between elements i and j . Leveraging the formulas from eqs. (11) and (12), the LCM
629 matrices are given by,

$$\bar{\mathbf{A}} = \begin{bmatrix} \overline{\rho c_p}_1 v_1 & 0 & 0 & 0 \\ 0 & \overline{\rho c_p}_2 v_2 & 0 & 0 \\ 0 & 0 & \overline{\rho c_p}_3 v_3 & 0 \\ 0 & 0 & 0 & \overline{\rho c_p}_4 v_4 \end{bmatrix}, \quad (67a)$$

$$\bar{\mathbf{B}} = \begin{bmatrix} \frac{1}{R_{12}} + \frac{1}{R_{14}} & -\frac{1}{R_{12}} & 0 & -\frac{1}{R_{14}} \\ -\frac{1}{R_{12}} & \frac{1}{R_{12}} + \frac{1}{R_{24}} + \frac{1}{R_{23}} & -\frac{1}{R_{23}} & -\frac{1}{R_{24}} \\ 0 & -\frac{1}{R_{32}} & \frac{1}{R_{32}} + \frac{1}{R_{34}} & -\frac{1}{R_{34}} \\ -\frac{1}{R_{14}} & -\frac{1}{R_{24}} & -\frac{1}{R_{34}} & \frac{1}{R_{14}} + \frac{1}{R_{24}} + \frac{1}{R_{34}} \end{bmatrix}, \quad \bar{\mathbf{f}} = \begin{bmatrix} \bar{q}^{(1)} \\ \bar{q}^{(2)} \\ \bar{q}^{(3)} \\ 0 \end{bmatrix} \quad (67b)$$

630 References

- [1] Adam J. Amar, A. Brandon Oliver, Benjamin S. Kirk, Giovanni Salazar, and Justin Drob. Overview of the charring ablator response (char) code. In AIAA, editor, *AIAA Aviation Forum*, 2016.
- [2] Guy L. Bergel, Frank B. Beckwith, Gabel J. de Frias, Kevin M. Manktelow, Mark T. Merewether, Scott T. Miller, Krishen J. Parmar, Timothy S. Shelton, Jesse T. Thomas, Jeremy T. Trageser, Benjamin T. Treweek, Michael V. Veilleux, and Ellen B. Wagman. *Sierra/SolidMechanics 5.6 User's Manual*, 2022.
- [3] Ricky T. Q. Chen, Yulia Rubanova, Jesse Bettencourt, and David Duvenaud. Neural ordinary differential equations, 2019.

- 640 [4] Jonathan Clausen, Victor Brunini, Lincoln Collins, Robert C Knaus, Alec Kucala,
641 Stephen Lin, Daniel Robert Moser, Malachi Phillips, Thomas Michael Ransegno,la,
642 Samuel Ramirez Subia, et al. Sierra multimechanics module: Aria verification manual-
643 version 5.22. Technical report, Sandia National Lab.(SNL-NM), Albuquerque, NM
644 (United States), 2024.
- 645 [5] Gary Cohen and Sebastien Pernet. *Finite Element and Discontinuous Galerkin Methods*
646 for Transient Wave Equations. Springer Dordrecht, Le Chesnay and Toulouse France,
647 2018.
- 648 [6] Matthew Gasch, Keith Peterson, Mairead Stackpoole, Ethiraj Venkatapathy, Gregory
649 Gonzales, and Kyle Hendrickson. Development of advanced ablative carbon phenolic
650 tps for future nasa missions and commercial space. In *38th Annual Small Satellite*
651 *Conference*, Logan, Utah, May 2024.
- 652 [7] Frank P. Incropera, David P. DeWitt, Theodore L. Bergman, and Adrienne S. Lavine.
653 *Fundamentals of Heat and Mass Transfer*. Wiley, Hoboken, NJ, 7th edition, 2011.
- 654 [8] R. J. Klock and Carlos Cesnik. Nonlinear thermal reduced-order modeling for hypersonic
655 vehicles. *AIAA Journal*, 55(7), 2017.
- 656 [9] Alberto Padovan, Blaine Vollmer, Francesco Panerai, Marco Panesi, Kelly A. Stephani,
657 and Daniel J. Bodony. An extended bformulation for ablating-surface boundary condi-
658 tions. *International Journal of Heat and Mass Transfer*, 218:124770, 2024.
- 659 [10] Eric Parish and Karthik Duraisamy. Non-markovian closure models for large eddy
660 simulations using the mori-zwanzig formalism. *Phys. Rev. Fluids*, 2:014604, Jan 2017.
- 661 [11] Eric Parish and Karthik Duraisamy. A unified framework for multiscale modeling using
662 the mori-zwanzig formalism and the variational multiscale method. *ArXiv*, 12 2017.
- 663 [12] Eric Parish and Karthik Duraisamy. *Coarse-Graining Turbulence Using the*
664 *Mori-Zwanzig Formalism*. Cambridge University Press, Cambridge, 2025.
- 665 [13] Carlos A. Vargas Venegas, Daning Huang, Patrick Blonigan, and John Tencer. Physics-
666 infused reduced-order modeling for analysis of multi-layered hypersonic thermal protec-
667 tion systems. *ArXiv*, 2025.
- 668 [14] Yin Yu, John Harlim, Daning Huang, and Yan Li. Learning coarse-grained dynamics
669 on graph. *arXiv preprint arXiv:2405.09324*, 2024.